Self-Assembly of Nanoparticles Functionalized with Mesogens

Haoliang Dong

Supervised by Dr. Xiangbing Zeng

Prof. Goran Ungar

A thesis Submitted for the Degree of Master of Philosophy

Department of Materilas Science and Engineering

University of Sheffield

November 2013

Acknowledgement

I would like to give sincere thanks to my respected supervisors Dr. Xiangbing Zeng and Professor Goran Ungan. They lead me to the mysterious liquid crystals world and teach me the genuine of the science. For their helpful advice, valuable guidance and encouragement throughout my whole MPhil study.

I would like to thank all the colleagues in my group. Their advice and support on life and academics, allow me a wonderful experience in Sheffield.

I would like to give my special thanks to the Department of Materials Science and Engineering for the scholarship to support me to fulfil the MPhil study here. For the kindly provided samples from Prof. Georg H. Mehl's group in the University of Hull, Dr. Liliana Cseh's group in the Institute of Chemistry Timisoara and Prof. Atsushi Muramatsu's group in the Tohoku University, I sincerely appreciate the help and offers. To all the technicians in the department, I just feel so grateful for the trainings I received on DSC, TEM and Coutour GT.

I would like to thank Diamond Synchrotron Radiation Source (U.K.) for providing the beamtime over the past year.

I would like to offer my genuine thanks to my parents for their understanding, support and care. It is with their love without reservation that I can overcome all the difficulties and challenges in my life.

Once again, thank all the people I met in Sheffield. It is you who make my MPhil so meaningful.

Abstract

Assembly on metallic nanoparticles has attracted great interest due to their wide potential applications in semiconductors and nanocatalysis. Recent theories also suggest that they have the promises in providing materials base for metamaterials with interesting optical properties such as negative refractive index. While most previous attempts to design metamaterials rely on top-down techniques, in contrast, the bottom-up approaches based on the self-assembly of nanoparticles provide feasible and promising alternatives. Due to the combination of order and mobility at the molecular level, liquid crystalline molecules are perfect candidates for the synthesis and self-assembly of nanomaterials. It has been demonstrated that by covering nanoparticles with liquid crystalline molecules, strong anisotropy could be induced to affect the packing geometry of spherical nanoparticles, and long-range order could be achieved. These successful attempts include covering nanoparticles with rod-like mesogens, discotic mesogens and bent-core mesogens.

In this thesis, nanoparticles covered with hemi-phasmids as well as dendrimeric liquid crystal forming molecules, and some relevant liquid crystal compounds have been comprehensively investigated by Small-angle X-ray Scattering (SAXS), Grazing Incidence Small-angle X-ray Scattering (GISAXS) and Polarized Optical Microscopy (POM). A number of 1-D lamellar, 2-D hexagonal columnar, and 3-D cubic nanostructures have been successfully achieved.

The electron density maps for those liquid crystalline phases are reconstructed based on the integrated diffraction intensities. The corresponding models of self-assembled nanostructures are proposed depending on the electron density maps and molecular structures. Molecular modelling and molecular dynamics simulation have been carried out to verify the credibility of proposed models.

Contents

Chapter 1 Literature review

1.1 Introduction to liquid crystals

1.1.1 Concept of liquid crystal

Liquid crystals (LCs) are an intermediate state of matter lying between crystalline solid and liquid, as schematically shown in Figure 1.1.[1] Compared to solid crystals, liquid crystals possess a higher intermolecular and intramolecular mobility, which means they have a certain degree of freedom of molecular rotation, translation or oscillation. Compared to isotropic liquids, the long-range positional and orientational orders of the crystal state are partly kept in liquid crystals. Liquid crystalline molecules could form different liquid crystalline phase depending on their degree of positional and orientational orders. Liquid crystalline phases are also called mesophases and molecules possessing liquid crystalline properties are known as mesogens.

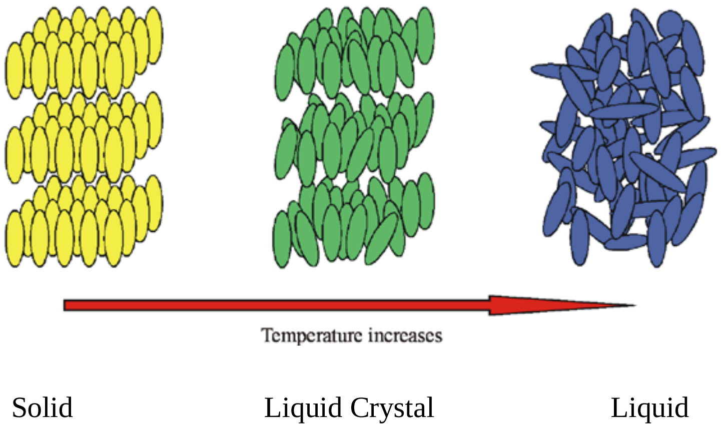

Figure 1.1 Transition from solid to liquid, through an intermediate liquid crystalline phase, of a rod-like molecule, at increasing temperature. The picture is taken from Dr. Feng Liu's PhD thesis, Ref. [2].

Not all molecules can form liquid crystalline phases, and the molecular shape and size play significant roles in the formation of them. First of all, the molecule must be anisotropic in its shape, e.g. be significant longer than it is wide. Secondly, the molecule must have some rigidity in its central region. That's reason why many liquid crystalline materials contain benzene rings.[3] Finally, that the ends of molecules are somewhat flexible would be advantageous in forming liquid crystal phases.[4] Such criteria work because anisotropic molecules bump into each other less if they tend to point in the same direction and flexible ends would allow molecules to position more easily with each other in an orderly way.

1.1.2 Typical liquid crystalline phases

The liquid crystalline state is a distinct phase of matter and possesses different types of structures depending on the amount of order in the material. Generally speaking, liquid crystals are categorized in two different ways depending on whether phase change is introduced by the temperature or the solvent, which results in two kinds of liquid crystals: thermotropic and lyotropic liquid crystals. In thermotropic liquid crystals, liquid crystalline phases exist in certain temperature regions. For lyotropic liquid crystals, the necessary condition for existence is a strong interaction of the polar compounds with the molecules of the solvent. Typically, the segregation of hydrophilic or hydrophobic regions of an amphiphilic molecule from a solvent provides the driving force for the forming of liquid crystalline phases.[5]

As mentioned above, LCs can be classified according to the molecular shape of mesogens. Molecules, except spherical ones, may possess two types of orders known as orientational and positional orders. Orientational order means molecules prefer to lie along a specific direction called director. On the other hand, positional order refers to the extent to which the position of an average molecule or a group of molecules shows translational symmetry.

Calamitic (rod-like) molecules mainly form nematic (N) and/or smectic phases (S_m). Rod-like molecules are elongated and linear, which consist of a rigid core with flexible chains attached to the each terminal end. The word nematic refers to thread-like defects often observed in such phases using Polarized Optical Microscopy (POM). The nematic liquid crystal phase is characterized by a long-range orientational order and the absence of any long-range positional order. In this case, rod-like molecules tend to point in the same direction called director. Because the nematic phase possesses high mobility of molecules which leads to its low viscosity, similar to that of isotropic liquids. But due to high contrast between the length and breadth of molecules, the nematic phase possesses high-degree of anisotropy.

Depending on the orientation order of the liquid crystals, different textures under polarized optical microscopy could be observed. In the liquid crystalline state, the anisotropy of macroscopic physical properties is due to the orientational order of anisotropic molecules (rod-like or disk-like mesogens). And the index of refraction is dependent on the polarization direction of the incident beam. So for the different orientational order of the liquid crystals examined using polarized optical microscopy, different textures could be obtained, some of them are so typical that they could be used to help identify different liquid crystalline phases.

Cholesteric state, also known as chiral nematic, exists in chiral compounds. In the cholesteric phase, the director is not fixed to a certain direction but tends to rotate through the sample. The director need to travel a certain distance to fulfil a full turn and the distance is called the "pitch" of the chiral nematic liquid crystal. Due to the twisted structure of the phase, interesting optical properties could be generated. For example, when the pitch equals to the wavelength of light, selective reflection can occur. Furthermore, such chiral compounds respond differently to right-handed and left-handed circularly polarized light, thus attract great interests e.g in making metamaterials.

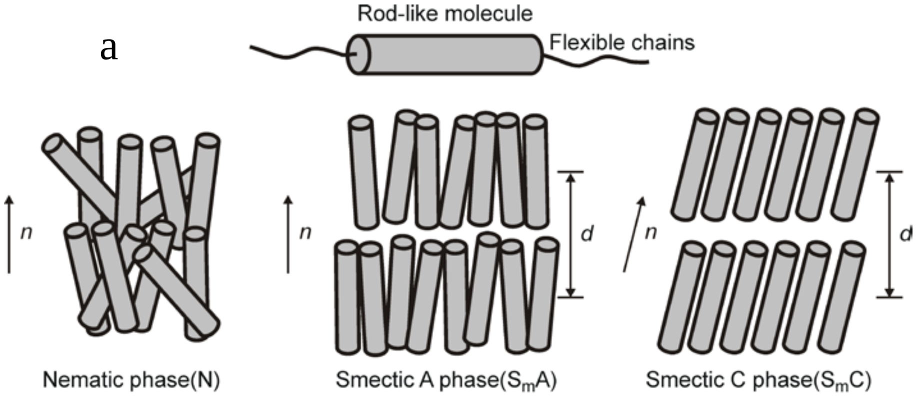

Figure 1.2 Mesophases formed by the organization rod-like molecules. The picture is taken from Dr. Feng Liu's PhD thesis, Ref. [2].

In the smectic phase, the molecules maintain the general orientational order as in nematics but in addition align themselves in layers or planes. Inside the layer, the molecules tend to point in the same direction. Except for the long-range translational order between layers, the molecules have the possibility for rotation and translation. And if the director is perpendicular to the smectic layers/planes, it is named as

Smectic *A* phase (S_mA). Otherwise the director is at a constant tilt angle to the semctic plane, it is called Smectic *C* phace (S_mC) as shown in Figure 1.2.

Discotic liquid crystalline mesogens, typically molecules consist of a disc-shaped aromatic core with hydrocarbon tails, can also form the nematic phase. The molecules move randomly in space but on average, the axis is mainly pointed at the same direction. In most cases, the molecules are packed one upon another to form columns. The effect of the flexible chain is quite important because it lowers the melting temperature and isolates neighbouring columns, thus provides freedom in the structure and mobility of molecules in it for the mesophases to form.

Generally the hydrocarbon chains are assumed to be liquid like and the column are further arranged together into 2-D lattice leading to columnar phase with hexagonal, rectangular or oblique symmetry (Figure 1.3).

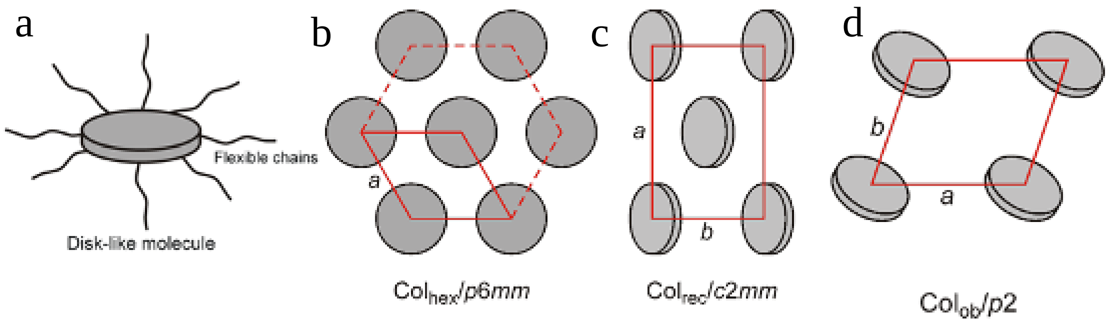

Figure 1.3 Schematic representation of a) disk-like molecule b) hexagonal columnar phase with *p6mm* symmetry; c) rectangular columnar phase with *c2mm* symmetry; d) columnar oblique phase. The picture is taken from Dr. Feng Liu's PhD thesis, Ref. [2].

Phasmidic and hemiphasmidic LCs are a relatively new family of thermotropic mesogens. Generally phasmidic mesogens consist of elongated rigid part and two peripheral half discs each substituted with three aliphatic chains. The name derived from the similarity of the molecule to stick-like insect called phasma. Hemiphasmidic mesogens contain only one half-disk and a rod-like moiety. The molecular structure of a hemiphasmid is shown in Figure 1.4. As an intermediate between rigid and flexible, rod-like and disk-like, much attention has been paid to their supramolecular structures. Liquid-crystalline polymers containing mesogentic units based on hemiphasmids can form either columnar hexagonal and double-layer smectic A or C mesophases.[6] Smectic, columnar and cubic mesophases have already been found in binary systems of hemiphasmidic and calamitic amphiphilic diols.[7] In this thesis work, we are also interested in investigating the mesophases formed by the hemiphasmidic compounds and hybrid systems of nanoparticles functionalized by them.

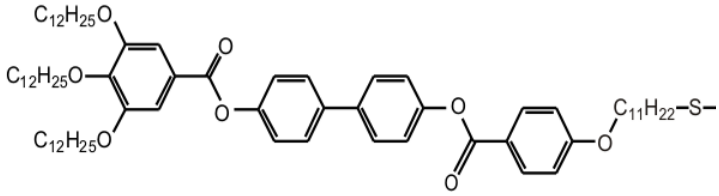

Figure 1.4 Molecular structure of a hemiphasmid.[8]

1.2 Self-assembly of nanoparticle – liquid crystal hybrid system

Assembly on metallic nanoparticles has attracted great research interest due to their wide applications in semiconductors[9] and nanocatalysis[10]. Recent theories also suggest that they have promises to provide the materials base for metamaterials with interesting properties such as negative refractive index.[11] While most previous attempts to design metamaterials rely on top-down techniques,[12] that is by slicing or etching a bulk materials to get nano-sized particles. However, the miniaturization is limited by using shorter wavelengths due to lens effects. In contrast, the bottom-up approaches based on the self-assembly of nanoparticles provide feasible and promising alternatives.[13] Cubic arrays have already been obtained by covering gold nanoparticles with DNA[14] to control their self-assembly. Attempts to order nanoparticles by grafting liquid crystalline moieties to the surface of nanoparticles are relatively recent.[15] Due to the combination of order and mobility at the molecular level, liquid crystalline molecules are perfect candidates for the synthesis and self-assembly of nanomaterials.[16] It has been demonstrated that by covering nanoparticles with liquid crystalline molecules, strong anisotropy could be induced to affect the packing geometry of spherical nanoparticles and long-range order could be achieved on the mesoscale.[17] These successful attempts include covering gold nanoparticles with rod-like mesogens[18], discotic mesogens[19] and bent-core[20] mesogens. This novel and exciting self-assembly behaviours of such systems reveal new doors to bottom-up design of metamaterials, at the same time they raise new questions in understanding the design principles for self-assembled nanoparticles in general. The understanding the mechanism and correlation between the number, shape and size of the liquid crystalline molecules attached to the nanoparticles are particularly important.

The combination of nanoparticles with liquid crystalline molecules can be generally classified into two categories: colloidal particle-liquid crystal system and mesogen functionalized nanoparticles. The first one is by dispersing nanoparticles into a liquid crystal host, and the second by grafting liquid crystalline molecules onto the surface of nanoparticles. Within metallic nanoparticles, gold nanoparticles are prime candidates due to their high stability and plasmonic resonance effects.

1.2.1 Colloidal Particle-Liquid Crystal System

The colloidal-liquid crystal systems have been investigated for many years, by dispersing colloidal particles in a matrix of liquid crystals, usually in the nematic phase.[16] The liquid crystalline molecules tend to align themselves along a preferred direction with respect to the surface of nanoparticles, inducing topological defects and other forces between the nanoparticles, which may lead to their orderly packing in such hybrid systems. Due to their anisotropy, the orientation of nematic phase could be easily changed by applied external electric or magnetic field. When colloidal is introduced to nematic liquid crystals, the orientation of nematic phase would be interfered. Structure forces would arise because of the elastic energy deformation resulted from the separation of inclusions. The structure forces are long-range in nematic liquid crystals and highly anisotropic, which reflects the order in liquid crystals.[21]

Figure 1.5 shows the interference when the colloid is placed into the nematic liquid crystals 5CB. Two different types of 2D nematic colloidal crystals with dipolar and quadrupolar symmetry were observed due to the balance between the minimized free energy by sharing topological defects and repulsive structure forces.

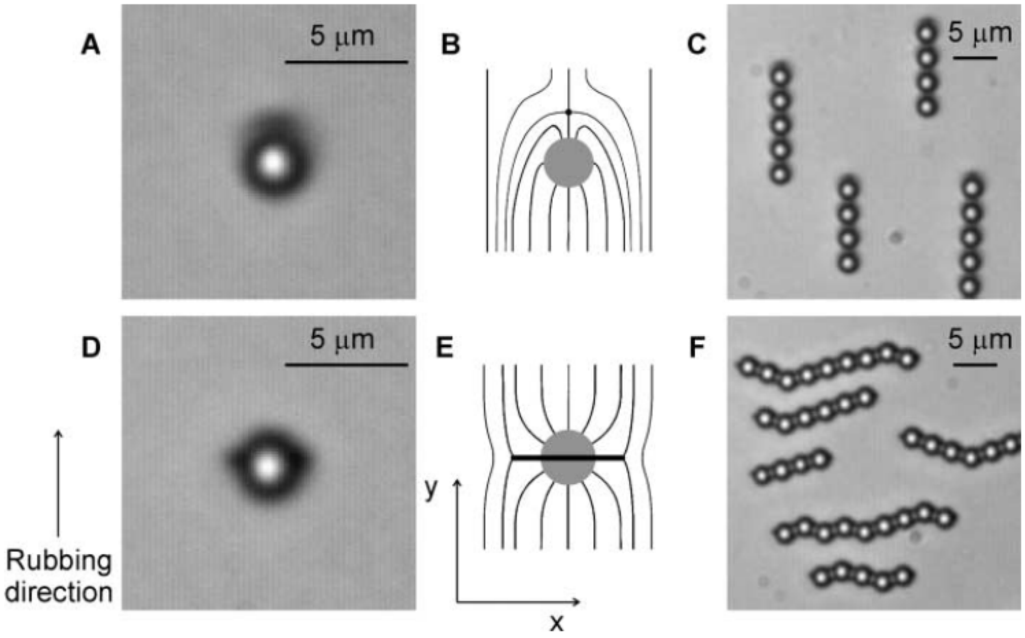

Figure 1.5 A) Micrograph of a *d* = 2.32 µm silica sphere in an *h* = 5µm layer of 5CB with a hyperbolic hedgehog defect. B) The nematic order of around the colloid C) Dipoles spontaneously form dipolar chains along the rubbing direction. D) The same type silica sphere in an *h* = 2.5µm layer of 5CB with Saturn ring. E) The nematic order of around the colloid. F) Quadrupoles spontaneously form dipolar chains perpendicular to the rubbing direction.[22]

1.2.2 Mesogen Functionalized Nanoparticles

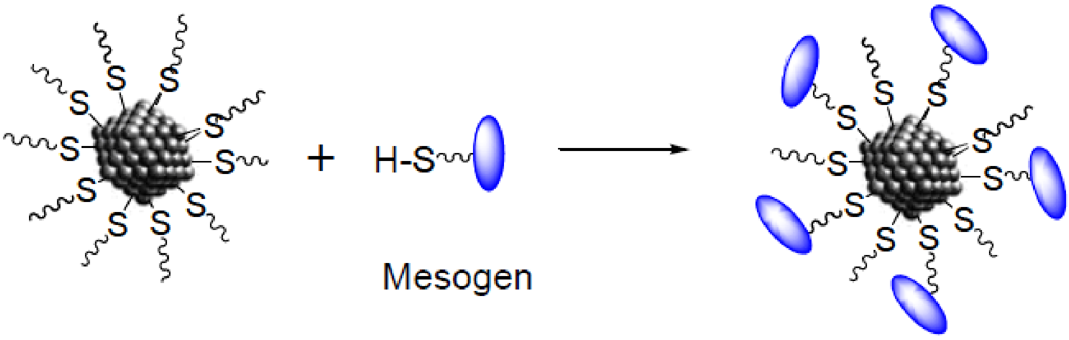

Figure 1.6 Schematic drawing of the synthesis of a side-attached mesogen functionalized gold nanoparticles. The picture is taken from Dr. Xiaobin Mang's PhD thesis, Ref.[23]

The nanoparticle functionalized with mesogens systems are gaining popularity because more complicated structures could be obtained and the size of the nanoparticles is relatively easy to control. The synthesis of nanoparticles hybrids varies mainly with the nature of the nanoparticles. In the case of gold nanoparticles, which have been well investigated, the synthesis of mesogen functionalized gold nanoparticles are usually in a two-step synthetic process as shown in Figure 1.6.[24] Firstly the gold nanoparticles, covered with a monolayer of hydrocarbon molecules with terminal thiol group, are synthesized. In the second step, the hydrocarbon coated gold nanoparticles react with the liquid crystalline molecules in an exchange reaction.[19] The number of mesogens attached to the nanoparticles could be controlled by changing reaction condition, so the gold nanoparticles could be coated completely or only partly by mesogens. The mesogens are also referred to as ligands and the remaining hydrocarbon chains are called co-ligands.

1.2.3 Rod-like mesogen covered gold nanoparticles

Rod-like molecules are the most commonly used to cover nanoparticls due to their easy availability and our thorough understanding of their liquid crystalline behaviour. Usually such rod-like mesogens are attached to gold nanoparticles through a flexible alkyl chain spacer (thiol ended normally to bond to the gold atom). And there are two ways that the mesogens can be connected to the spacer, at the end or at the side. The flexibility of the rod-like ligands in hybrid systems play a significant role in forming the mesophases because they allow the hybrid particles to be anisotropic in their shape.

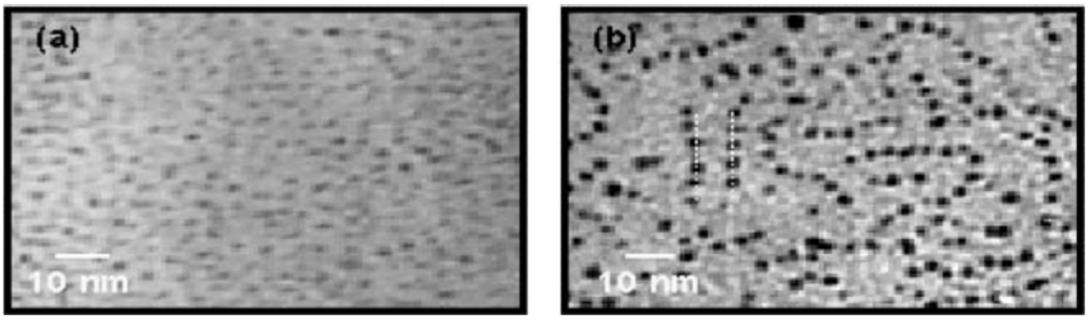

Figure 1.7 TEM images of gold nanoparticles with liquid crystal ligands (a) before and (b) after thermal treatment.[18]

Some interesting research results on rod-like molecules attached to gold nanoparticles have already been obtained. 1-D lamellar ordering of the gold nanoparticles was achieved by grafting them with a liquid crystalline ligand, 4’-(12-mercaptododecyloxy)biphenyl-4-carbonitrile.[18] The ligand was end-attached to the surface of the gold nanoparticles via a thiol group. Through annealing of the sample followed by quenching to room temperature, direct observation of 1-D lamellar structure was achieved on a TEM grid, in line with Small-angle X-ray Scattering (SAXS) results (Figure 1.7). Two layers of liquid crystalline mesogens comprise the inter-array regions, and the self-assembly of smectic liquid crystalline molecules is crucial for forming such a mesophase.

Relevant research has been continuously carried out in our group. By coating gold nanoparticls with laterally attached nematic liquid-crystal-form ligands, 2-D columnar hexagonal and 3-D rhombohedral phase could be obtained.[25] In both cases, nanoparticles were arranged into columns. And the volume fraction of co-ligand in nanoparticle-liquid crystal hybrid systems could be used to control the anisotropy of self-assembly of gold nanoparticles.[26] Neither too large nor too small volume fraction of co-ligand of systems could achieve the anisotropic mesophases.

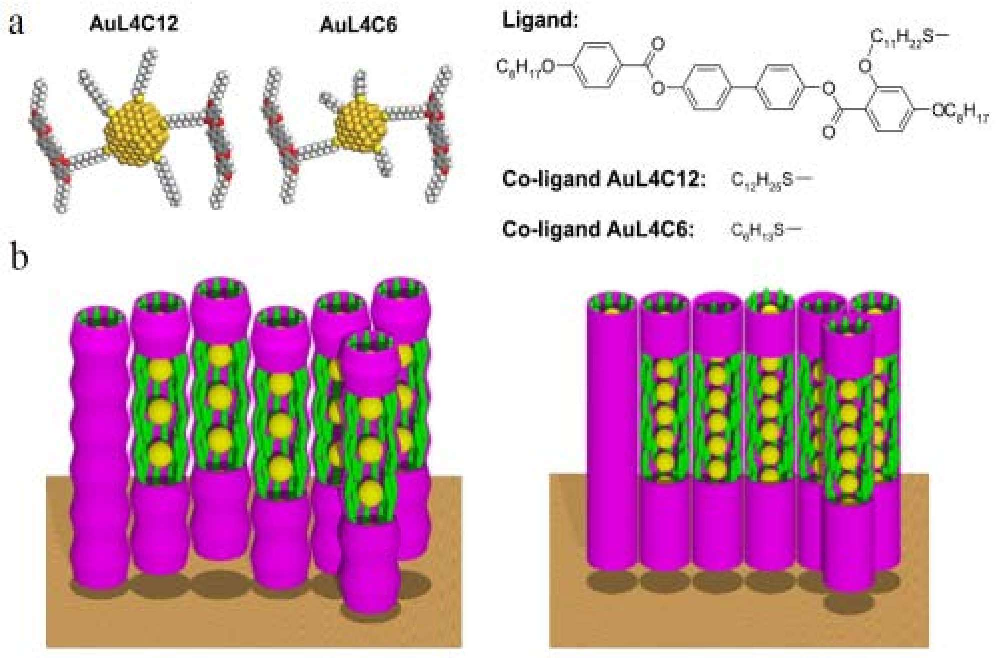

Figure 1.8 a) Schematic structure of gold nanoparticles covered with laterally attached ligand and co-ligand b) Schematicl models of the gold string structures. Left: Rhombohedral phase in AuL4C12. Right: Hexagonal columnar phase in AuL4C6. Yellow balls and green strings represent gold nanoparticles and mesogens respectively.[16]

Highly ordered 2-D and 3-D structures were also found in nanoparticle covered with laterally attached rod-like nematogenic mesogen by controlling the co-ligand length.[25] Interestingly, Small-angle X-ray Scattering (SAXS) analysis in both cases indicated the nanoparticles were arranged into columns. The proposed 2-D and 3-D models were schematically shown in Figure 1. 8b. For gold nanoparticles covered with ligand containing quaterphenyl and dodecylthiol co-ligand (AuL4C12), 3-D rhombohedral lattice with space group *R3m* was found as indicated in the GISAXS pattern. The column was arranged in a triangular lattice with three columns placed along the *z*-axis by 0, c/3 and 2c/3 respectively. And for gold nanoparticles functionalized by shorter hexylthiol co-ligand (AuL4C6), 2-D rectangular and hexagonal columnar mesophases were obtained as columns formed in AuL4C12. It is interesting to note that in both cases, the POM textures were typical Schlieren type, normally observed for nematic phases. This is attributed to the fact that the organization of the LC molecules in such 2D and 3D structures are more similar to that of a nematic phase, and the laterally attached rod-like mesogens provided a strong orienting influence on the arrangement of gold nanoparticles.

Further investigation indicated that the self-assembly of gold nanoparticles can be controlled by attaching mesogens of different sizes and changing the length and number of co-ligands. The volume fraction of the co-ligand in these systems is crucial for controlling the anisotropy of self-assembly of gold nanoparticles.[26] For gold nanoparticles covered with triphenyl and no aliphatic co-ligand (AuL3), 3-D hexagonal phase could be obtained with nearly the same parameter *a* and *c*. No birefringence could be observed due to the lack of long-range orientational order of mesogens as the attached ligand need to follow the curvature of nanoparticles. For gold nanoparticles (AuL3C6) covered with mixture of triphenyl and co-ligand, $C_6H_{13}SH$, 2-D hexagonal structure could be obtained. For AuL3C12 with longer aliphatic co-ligand, after chloroform vapour treatment, face-centred cubic (FCC) lattice was obtained, which in consistent with lack of birefringence in FCC system.

1.2.4 Rod-like mesogen covered silsesquioxane

Silsesquioxanes are organosilicon compounds with empirical chemical formula $RSiO_{3/2}$, , which could have a cage-like structure as shown in Figure 1.9. A silsesquioxane has a stable and compact chemical structure and the stable cubic structures could be modified by attaching different mesogeons of different shape and size, to the silicon atoms at corners.[27]

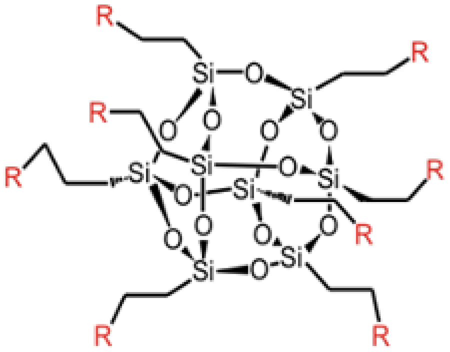

Figure 1.9 Molecular structure of silsesquioxane cages

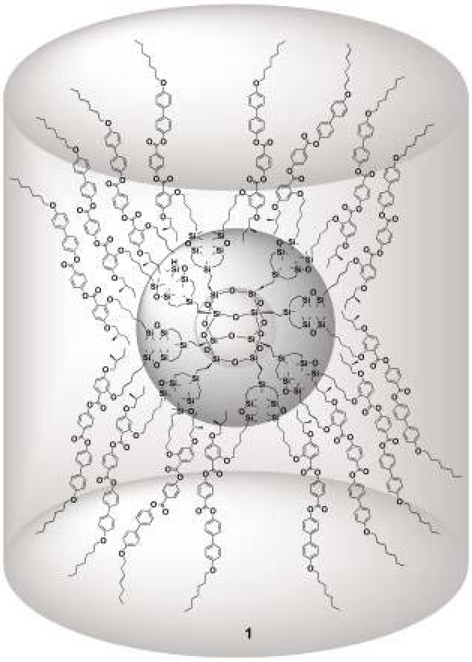

Figure 1.10 Schematic model of dendrimerized silsesquioxance.[27]

Silsesquioxane functionalized mesogens are appearing because all the connections between organic and inorganic compounds are via covalent bonds, which leads to the précised defined interfacial interactions and topologies.[27] Chrial nematic and columnar mesophases were observed in the silsesquioxane coated with dendrimers,[28] synthesized through hydrosilylation exchanging reaction. The dendrimers based on the silsesquioxane core are drawn in Figure 1.10. Powder X-ray diffraction confirmed that the structures converted from hexagonal columnar phase at high temperature to rectangular columnar mesophase when cooled down.

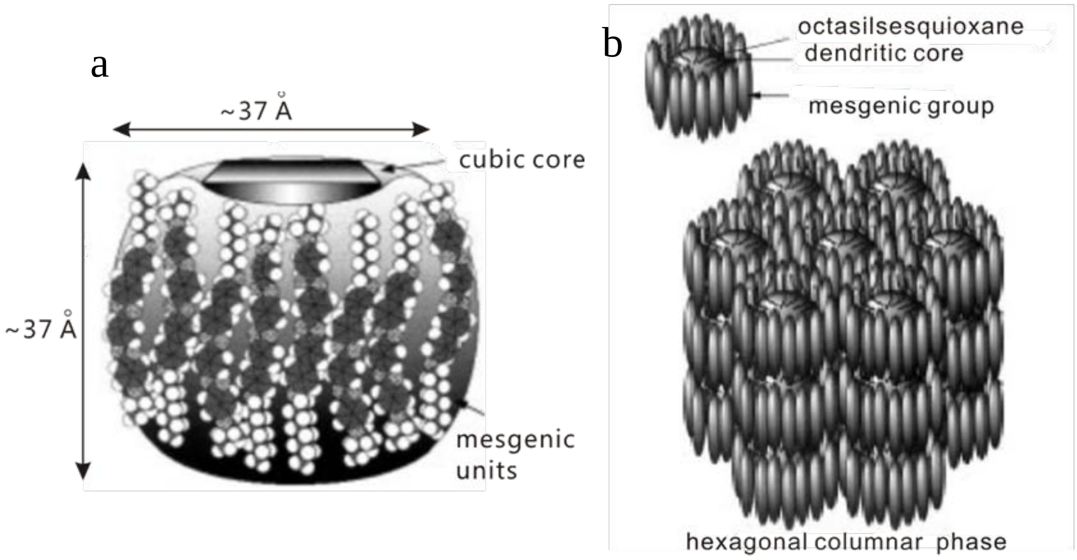

Figure 1.11 a) Schematic model of the conformational structure of dendritic disk. b) The proposed model on the hexagonal columnar phase. [28]

The model of the columnar mesophases suggested that the dendrimer had a disk-like gross molecular shape. As the inter-columnar space was too small for dendrimers to be arranged, dendritic disk might be arranged into a wheel (Figure 1. 11a). In the hexagonal columnar phase, the silsesquioxane core were stacked along the column axis and the attached dendrimers laid in a disordered way in the inter-columnar space.

1.2.5 Discotic mesogen covered nanoparticles

The discotic mesogens have also been used to coat nanoparticles, due their ability to pack one upon another to form columns, with potential applications e.g. as electrical conduction channels along the column axis.[29]1-D lamellar, 2-D hexagonal columnar and disordered structure were obtained in gold nanoparticles covered with a triphenylene (TP) moiety by controlling the degree of π-π interaction among triphenylenes around the nanoparticles.[30] The strategies to control the free space around triphenylene ligand were by reducing the core size or using the long alkyl chain as the spacer as shown in Figure 1.12.

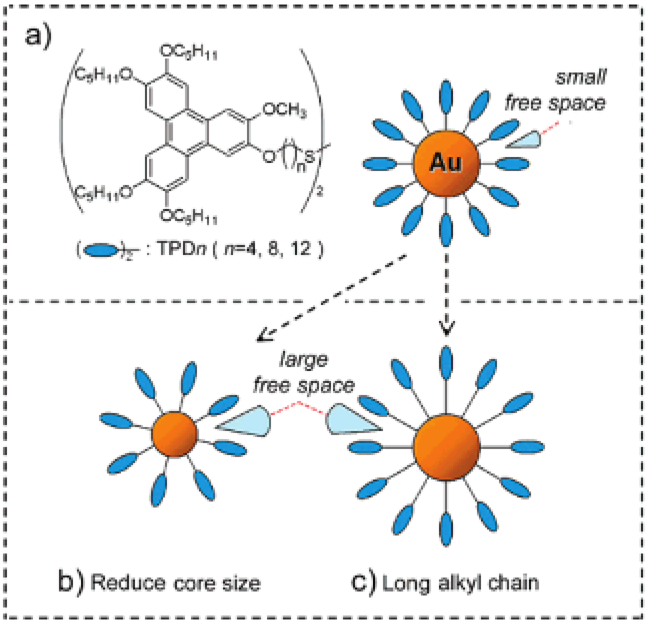

Figure 1.12 a) Schematic model of gold nanoparticles covered with disk-like mesogens; Control the free space around triphenylene moieties: b) reduce core size c) use long alkyl chain.[30]

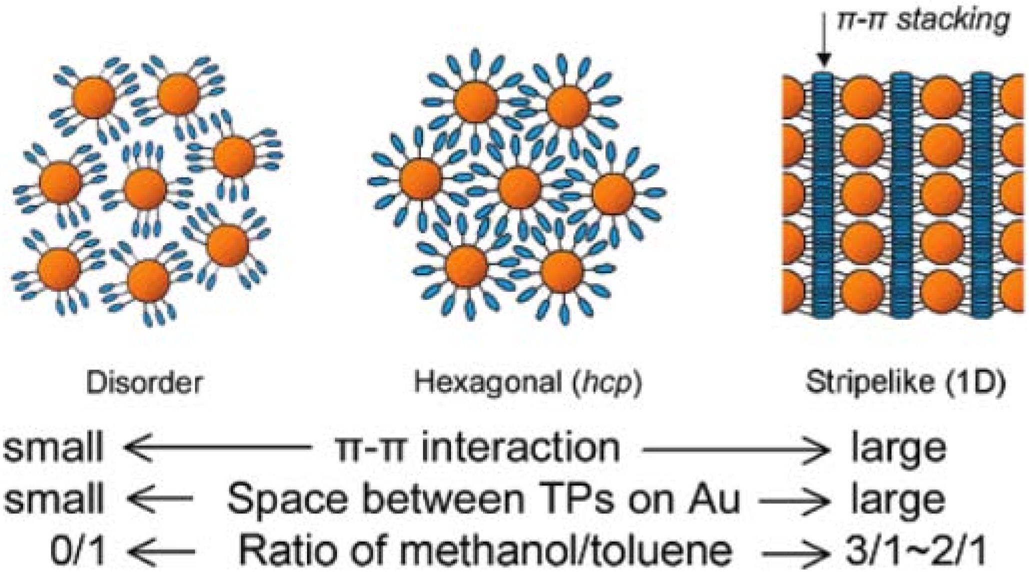

Figure 1.13 The proposed model of gold nanoparticles covered with triphenylene by changing the degree of π-π stacking.[30]

As shown in Figure 1.13, the π-π stacking of the triphenylene legands played a significant role in forming the long-range order of liquid crystalline phases. Sufficient free space among the triphenylene ligands would allow easy insertion of triphenylenes which resulted in strong interparticle *π-π* interaction to form ordered structures. Besides, the gold nanoparticle arrangement could also be tuned by adjusting the polarization of solvents through changing the ratio between methanol and toluene as a result of competing intermolecular stacking interactions of triphenylene (TP) moieties among gold nanoparticles with TP. With the hydrophilicity of the solvent increasing by adding more methanol, the stacking was converted from the hexagonal close packed structure at low ratio of methanol to toluene (0/1, 1/1) to a stripelike arrangement at high ration of 3/1. The hydrophilicity of the solvent could help develop strong intermolecular interactions of the triphenylene ligands, leading to the formation of mesophases.

1.2.6 Dendrimers covered nanoparticles

Dendrimers are a relatively new family of the thermotropic mesogens and consist of branched molecules attached to a central core. And the branching unit, also known as dendrons, usually have functional groups at the terminal ends. Functional groups can be inserted at specific positions of the dendrimer, and they provide basis for controlling over the molecular architecture and microenvironment.[4] Consequently such compounds have high potential for various applications such as catalysis and nanomedicines.[29] The first synthesis and characterization of gold nanoparticle-dentrimer hybrid system was reported in 2007, where 2-D hexagonal and 3-D cubic structures were obtained.[31] In this case, the gold nanoparticles had an average size of 21 Å, comparable to that of the second generation dendrons attached to them as shown in Figure 1.14. The added dodecyl chain as the spacer of dendritic part could help increase the flexibility. The rigid aromatic dendritic cores are with cone-like conformations which will enhance the interparticle interactions and maintain the stability of mesophases. In the 3-D cubic arrays at high temperature, each unit cell consisted 3-D packing of a single type of pseudospherical decoreated gold nanoparticles, , with one located at the corner and the other at the body centre of the cubic unit cell. The proposed model of the cubic arrays is shown in Figure 1.15.

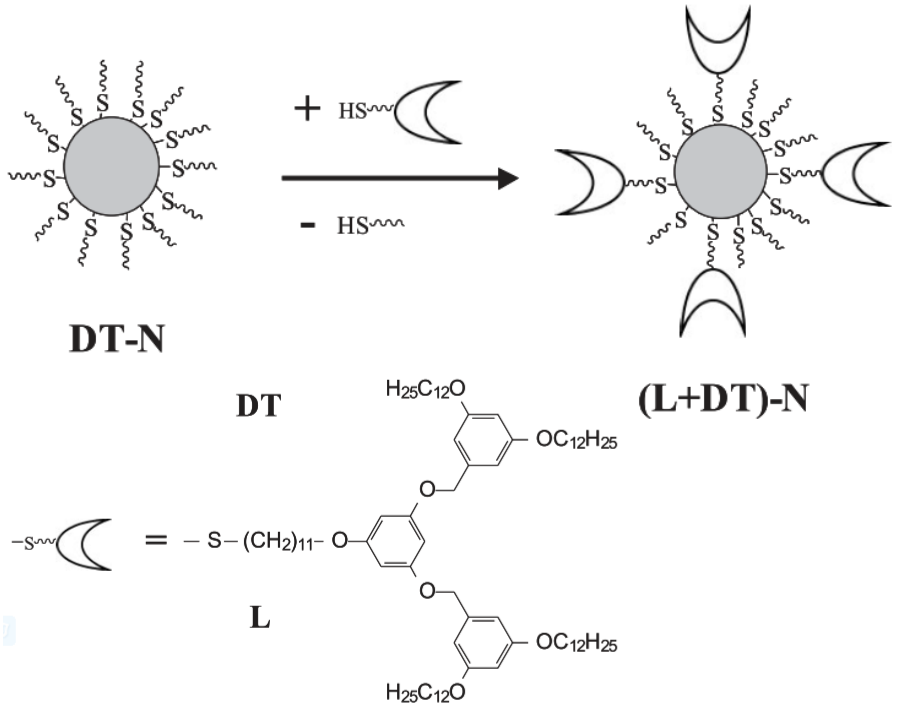

Figure 1.14 Schematic ligand exchange reaction yielding dendronized gold nanoparticles.[31]

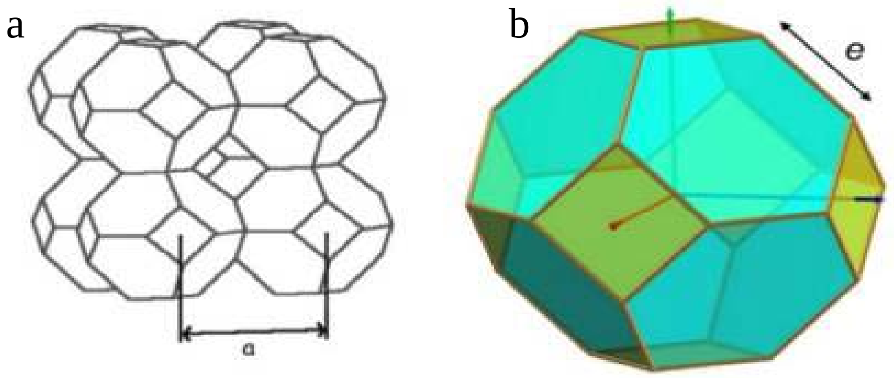

Figure 1.15 a) Schematic model of body centred cubic lattice composed of truncated octahedrons where *a* is the cubic lattice parameter. b) Schematic model of the truncated octahedron packing of gold atoms. [31]

3-D simple cubic packing of gold nanoparticles were achieved by grafting supramolecular dendrimeric corona through amidation to the carboxylic groups at the surface.[32] A series of dendrons G1, G2 and G3 shown in Figure 1.16 a were grafted to surface of gold nanoparticles A1, A2 and A3 with mean size of 5.9 ± 0.6, 6.8 ± 0.7 and 6.8 ± 0.8 nm, respectively. When cast from the toluene, a well-ordered hexagonal mododomain could be observed in Transmission Electron Microscopy (TEM) with an interparticle distance of 14nm in G2/A2 shown in Figure 1.16 b. After G2/A2 annealing at 150 °C, sharp peaks were observed in Small-angle X-ray Scattering (SAXS) which suggested the simple cubic phase shown in Figure 1.16 c. And the Figure 1.16d showed that the Grazing Incidence Small-angle X-ray Scattering (GISAXS) again confirmed the simple cubic phase with good orientation after annealing at 170 °C. As sharp peaks were only observed in G2/A2 while only amorphous structures with short-range order were produced in other combinations, it suggested the grafting density of G2 on A played a significant role in ordered structure forming.

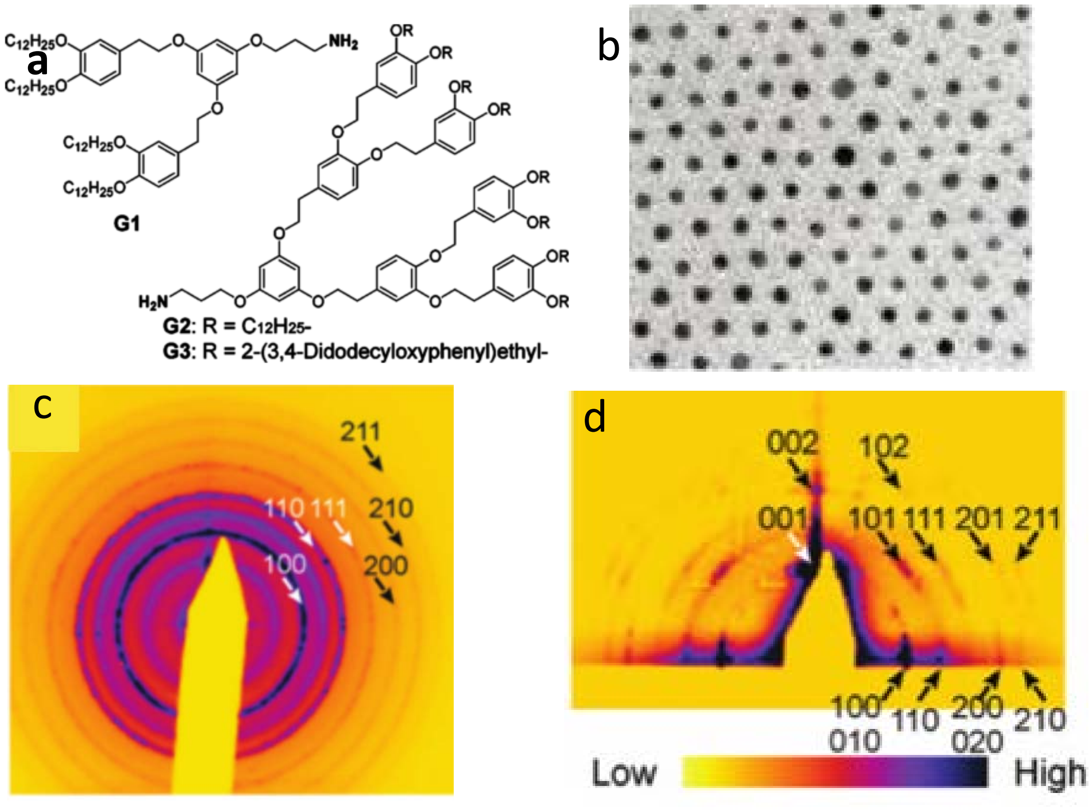

Figure 1.16 a) Molecular structure of dendrons used to cover gold nanoparticles. b) TEM image of G2/A2 c) SAXS pattern of G2/A2 at 150 °C d) GISAXS pattern of G2/A2 at 170 °C.[32]

1.3 Aims and objectives

The novel and exciting self-assembly behaviour of mesogen covered nanoparticles open new doors to bottom-up design of metamaterials, and for the understanding of their design principles. This project aims to improve our understanding of the mechanism and correlation between the number, shape and size of the liquid crystalline molecules attached to the nanoparticles.

In this project, the main research objectives are to solve the complex 1-D, 2-D and 3-D mesophases formed by the self-assembled nanoparticles covered with hemiphasmids and dendrons. This main investigation methods used include Small-angle X-ray Scattering (SAXS), Grazing Incidence Small-angle X-ray Scattering (GISAXS) and Polarized Optical Microscopy (POM).

The principles of the techniques as well as the procedures of reconstruction of electron density map and molecular dynamics simulations are described in details in Chapter 2. Chapter 3 explores the mesophases of the pure hemiphasmids at first and then focuses on the self-assembled structures formed by gold nanoparticles as well as silsesquioxane covered with hemiphasmids. Chapter 4 examines the mesophases formed by rod-like molecule DBCH, while Chapter 5 focus on dendronized Cadmium Sulphide (CdS) nanoparticles. Chapter 6 mainly deals with the mesophases of a disc-like compound containing gold atoms in the core: triangular pyridine-Au. Different nanostructures obtained in these systems are reported and experimental results discussed, followed by future work.

CHAPTER 2 Experimental

2.1 Small Angle X-ray Scattering

2.1.1 The Principle of Small-angle X-ray Scattering

X-ray is an electronmagnetic wave with wavelength at the order of angstrom, which is almost the same dimension of interatomic distance in crystals. X-ray diffraction is a non-destructive analytical method and plays a significant role in studying crystal structures and chemical compositions. The diffraction of X-rays by a crystal is generated by constructive interference of reflections by lattice planes of the crystal. As shown in Figure 2.1, diffraction happens when reflected waves from consecutive lattice planes have exactly the same phase, i.e. the path length difference (BCD in Figure 2.1) is an integeral multiply of the x-ray wavelength. It can be expressed by the Bragg's law[33]:

$$n\lambda=2d\sin\theta \tag{2.1}$$

Where θ is the of the diffraction angle, d is the interplannar spacing, and n the order of diffraction.

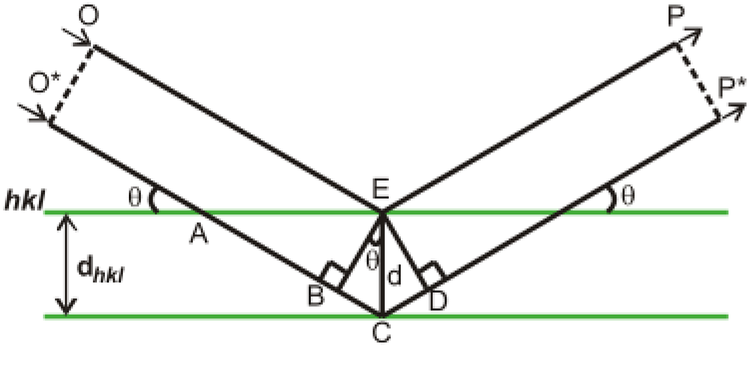

Figure 2.1 Bragg's law. The difference between two path lengths OEP and O*CP* equals BCD=$2d\sin\theta$, the condition for diffraction then requires, $2d\sin\theta=n\lambda$.

Figure 2.2 shows that a parallel incident X-ray beam is scattered by two electrons located at O and P which are at the distance represented by the vector $\vec{r}$. A fraction of the incident beam would be scattered at the angle θ. θ is half of the scattering angle.

Vector $\vec{s}_0$ and $\vec{s}$ are used to indicate the direction of the incident and scattered beam, respectively.

Consequently the path difference between the point O and R can be expressed as[25]:

$$\vec{r} \cdot (\vec{s} - \vec{s}_0) \tag{2.2}$$

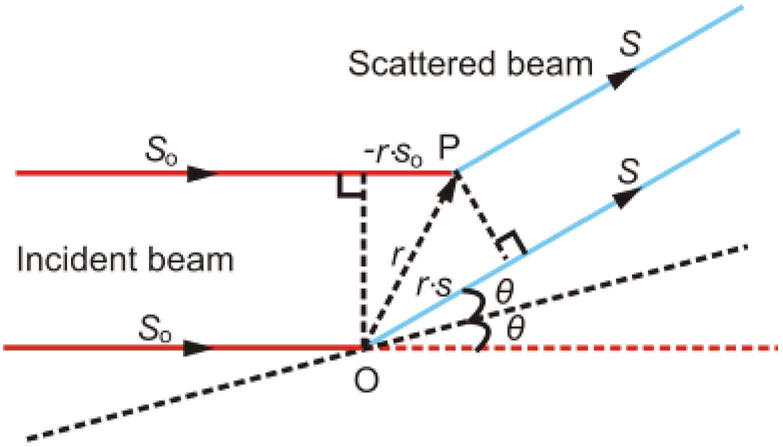

Figure 2.2 Scattering by two electrons at the point P and O

And hence the phase difference is:

$$(2\pi/\lambda) \cdot \vec{r} \cdot (\vec{s} - \vec{s}_0) \tag{2.3}$$

A vector $\vec{q}$ is defined by:

$$\vec{q} = (2\pi/\lambda) \cdot (\vec{s} - \vec{s}_0) \tag{2.4}$$

Then the $\vec{q}$ vector has the same direction as *s* with magnitude of :

$$|q| = \frac{4\pi}{\lambda}\sin\theta \tag{2.5}$$

In this case, the phase difference between the two scattering waves can be simplified as $\vec{r} \cdot \vec{q}$.

The scattering intensity of one single free electron:

$$I_e = I_0 \frac{e^4}{m^2c^4R^2} \frac{1+\cos^2 2\theta}{2} \tag{2.6}$$

Where I_o is the intensity of the incident X-ray beam and μ_0 and *e* are constants. *m* is the mass of electron, *p* is the polarization factor and depends on the polarization of the incident beam and scattering angle. For Small-angle X-ray Scattering *p* is equal to 1. For polarized and unpolarized X-ray beam, the polarized factor *p* could be expressed as:

$$\text{p} = \begin{cases} \cos^2 2\theta \ldots\ldots\ldots \text{Polarisation perpendicular to plane of scattering} \\ 1 \ldots\ldots\ldots\ldots\ldots\ldots\ldots\ldots\ldots\ldots\ldots \text{Polarisation in Plane of scattering} \\ \dfrac{1+\cos^2 2\theta}{2} \ldots\ldots\ldots\ldots\ldots\ldots\ldots\ldots\ldots\ldots\ldots \text{Unpolarised X-rays} \end{cases} \tag{2.7}$$

If *ρ(r)* is defined as the electron density at position P, the number of the electrons in the volume will be *ρ(r)* · *dv*. The amplitude scattered at angle 2θ, or corresponding wave vector ***q***, by these electrons could be written as:

$$F(\boldsymbol{q}) = \int_V \sqrt{I_e}\,\rho(\boldsymbol{r})\exp(i\boldsymbol{q}\cdot\boldsymbol{r})dv \tag{2.8}$$

In this project, only the relative intensities of the X-rays scattered needs to be considered as we do not measure the absolute intensity. Therefore, the resultant scattered wave at the angle 2θ can be simplified as：

$$F(\vec{\boldsymbol{q}}) = \int_V \rho(\vec{\boldsymbol{r}})\exp(i\vec{\boldsymbol{q}}\cdot\vec{\boldsymbol{r}})dv \tag{2.9}$$

Therefore, the overall diffraction intensity could be written as:

$$I(\vec{q}) = I_e\cdot|F(\vec{q})|^2 = I_e\cdot|\int \rho(\vec{r})\cdot\exp(i\vec{q}\cdot\vec{r}_j)dv\,|^2 \tag{2.10}$$

If we define the unit vectors $\vec{s}_0$ and $\vec{s}$ with the magnitude of 1/λ, then the constructive inference of scattered beams occurs only when $\boldsymbol{r}\cdot(\boldsymbol{S}-\boldsymbol{S}_0)=m$ where *m* is the integer. If we define the lattice with unit vectors *a*, *b* and *c*, then we could come up with：

$$\begin{aligned} (\boldsymbol{S}-\boldsymbol{S}_0)\cdot\boldsymbol{a} &= h \\ (\boldsymbol{S}-\boldsymbol{S}_0)\cdot\boldsymbol{b} &= k \\ (\boldsymbol{S}-\boldsymbol{S}_0)\cdot\boldsymbol{c} &= l \end{aligned} \tag{2.11}$$

Where the *h*, *k* and *l* are integrals. This means the constructive inferences could occur when the equation 2.11 is satisfied.

Here we introduce a new set of lattice defined as the reciprocal lattice with unit vectors ***a****, ***b**** and ***c**** with the relationship with real space vectors *a*, *b* and *c* based on:

$$\begin{aligned}\boldsymbol{a}^{*}\cdot\boldsymbol{a}=1,\boldsymbol{a}^{*}\cdot\boldsymbol{b}=0,\boldsymbol{a}^{*}\cdot\boldsymbol{c}=0\\ \boldsymbol{b}^{*}\cdot\boldsymbol{a}=0,\boldsymbol{b}^{*}\cdot\boldsymbol{b}=1,\boldsymbol{b}^{*}\cdot\boldsymbol{c}=0\\ \boldsymbol{c}^{*}\cdot\boldsymbol{a}=0,\boldsymbol{c}^{*}\cdot\boldsymbol{b}=0,\boldsymbol{c}^{*}\cdot\boldsymbol{c}=1\end{aligned} \qquad (2.12)$$

Therefore the equation 2.11 could be simplified and a general solution could be shorten as:

$$(\boldsymbol{S}-\boldsymbol{S}_0)=h\boldsymbol{a}^{*}+k\boldsymbol{b}^{*}+l\boldsymbol{c}^{*} \qquad (2.13)$$

Where integers h, k and l are defined as the Miller indices of a plane (h, k, l) in real space.

Based on equation 2.13, the equation 2.8 could be rewritten as :

$$F(h,k,l)=\int_V p(x,y,z)e^{2\pi i s\cdot r}\,dv=\int_V p(x,y,z)e^{2\pi i(hx+hy+lz)} \qquad (2.14)$$

Where the structure factor F could, in one given *(hkl)* direction could be seen as the Fourier transform of the electron density within the system. Since the Fourier transformation is reversible, the electron density $\rho(x,y,z)$ is the inverse Fourier transform of structure factor so that electron density $\rho(x,y,z)$ could be expressed as :

$$\rho(x,y,z)=\sum\nolimits_{h,k,l}\left|F(h,k,l)\right|\exp[-2\pi i(hx+ky+lz-\phi_{h,k,l})] \qquad (2.15)$$

Where $\phi_{h,k,l}$ is the phase angle of the structure factor. Because the phase angle $\phi_{h,k,l}$ could not be obtained experimentally, that is the well-know "phase problem" in x-ray crystallography.

If a structure is centrosymmetric, the electron density $\rho(x,y,z)$ would equal $\rho(-x,-y,-z)$. And then structure factor of any given (h, k, l) index would be real. In this project, most of the systems are centrosymmetric. Therefore, the equation 2.15 could be simplified as:

$$\rho(x,y,z)=\sum\nolimits_{h,k,l}\left|F(h,k,l)\right|\cos[2\pi(hx+ky+lz-\phi_{h,k,l})] \qquad (2.16)$$

where the phase angle $\phi_{h,k,l}$ is either 0 or π.

2.1.2 Experimental Set-up of Small-angle X-ray Scattering

For liquid crystals, the periodicities exist between molecular moities, hence such structures are characterized by larger unit cells and the X-ray scattering peaks are observed in the small angle region. In this project, Small Angle X-ray Scattering (SAXS) is the main method to study liquid crystal structures, complementary by Wide Angle X-ray Scattering (WAXS).

The SAXS diffraction experiments on power samples are carried our on a lab machine as shown in Figure 2.3. A microfocus X-ray source (Cu-K_α radiation), coupled with an Xenocs multilayer mirror with a long focal length (FOX2D_Cu 12_INF) and two sets of slits is used to generate a low divergence beam, with a spot size of 0.8 mm x 0.8 mm at the sample position.

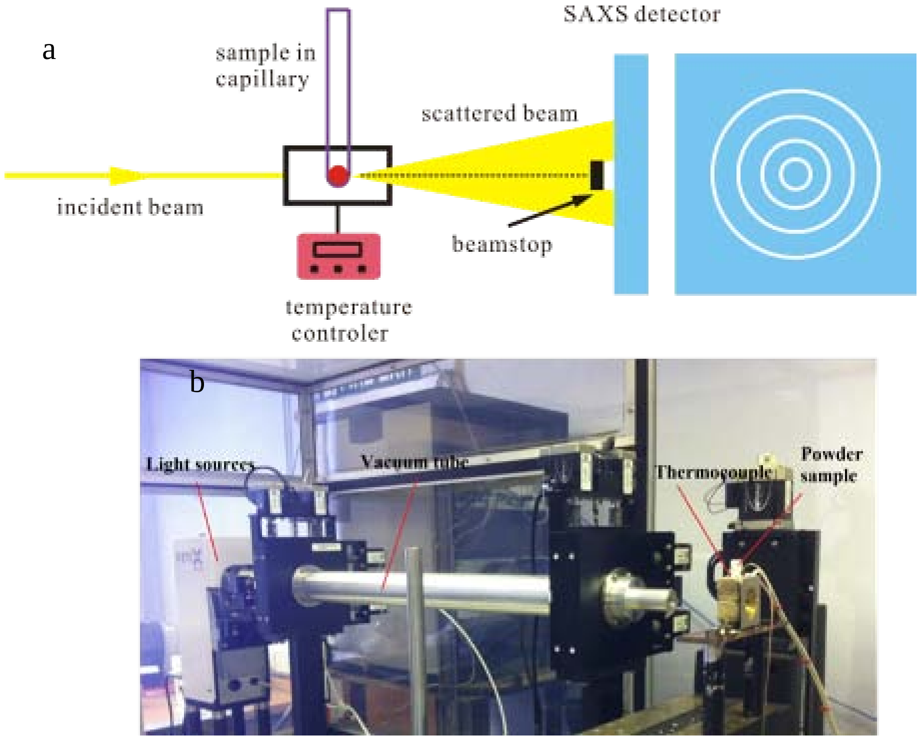

Figure 2.3 The set-up of Small-angle X-ray Scattering. a) Sketched set-up b) Real set-up

Powder samples are in 1mm glass capillaries, which are placed in a heating cell for temperature control. The diffraction patterns were recorded using a 2D Vantec 2000 detector and converted to 1D diffractograms using FibreFix (CCP13) software. The sample to detector distance is calibrated with a long paraffin ($C_{40}H_{82}$) with known d-spacings.

2.2 Grazing Incidence Small Angle X-ray Scattering

2.2.1 The principle of Grazing Incidence Small Angle X-ray Scattering

Grazing Incidence Small Angle X-ray Scattering (GISAXS) is a scattering technique to study nano-structured surface and thin films. As a hybrid technique, GISAXS combines concepts of transmission SAXS and the surface sensitivity of grazing incidence diffraction (GID). Like SAXS, it uses the form factor and structure factors; like GID, it uses scattering geometry close to the critical angles of substrate and film, and two-dimensional character of the scattering.

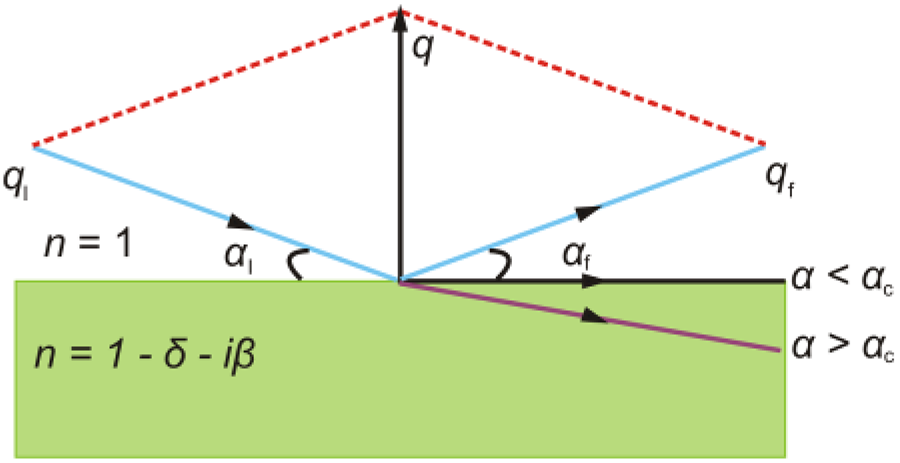

Figure 2.4 The X-ray reflective geometry.[2]

The X-ray refraction index is shown as[21],

$$n = 1 - \delta - i\beta \tag{2.17}$$

Where

$$\delta = r_e \rho_e \lambda^2 / 2\pi \tag{2.18}$$

Where r_e is the radius of electron and ρ_e is the average electron density, and

$$\beta = \mu\lambda/4\pi \tag{2.19}$$

Where λ is the wavelength of X-ray, μ is the absorption coefficient. Because δ and β are less than 10^{-5}, the X-ray reflection index is slightly less than 1. Therefore critical angle of total internal reflection could exist. The X-ray reflective geometry is shown in Figure 2.4.

As for GISAXS experiment, a thin film is prepared on the substrate so two interfaces, air/sample and sample/substrate, result in two critical angles. If the incident angle is larger than both, the incident beam could penetrate the thin film and the substrate. Thus the obtained diffraction pattern is resulted from the scattering of the primary beam. If the incident angle is lower than the first critical angle, which meets the condition of total reflection, very weak scattering pattern could be obtained. If the incident angle is in between, the diffraction pattern comes from both of the primary and reflected beam which reflects from the substrate surface. So the splitting of diffraction peaks along the perpendicular direction would appear in the scattering pattern.

GISAXS has several practical advantages. The first is that it is non-destructive method as well as SAXS. The second is that the sample preparation (by casting from solution or directly from melt) is relatively easy. The third one is that it could provide information on orientation geometry and size distributions which could simplify the indexing procedure. However, what makes GISAXS so useful in study of liquid crystals is because of the mobility and packing of liquid crystal molecules on the surface, which could generate preferred orientation along the surface normal. Consequently, in such well-oriented samples diffraction spots, instead of rings normally obtained for a powder sample, are observed. Important information of the geometrical relation between different diffraction peaks can be retrieved and could hugely facilitate the indexing of complex diffraction patterns.

2.2.2 Experimental Set-up of Grazing Incidence Small-angle X-ray Scattering

Synchrotron radiation is one particular type of cyclic particle accelerator originating from electron beam under magnetic field. The speed of the accelerated electrons could reach close to that of light and the x-rays emitted is much more intense compared with conventional x-ray tubes. Consequently it could generate excellent resolution within seconds so that dynamic evolution could be measured in rapid time series. Grazing Incidence Small-angle X-ray Scattering (GISAXS) in this project is the main complementary technique to normal Small-angle X-ray Scattering (SAXS). It is used in many cases to double check the indexing of diffraction patterns obtained from SAXS on powder sample. More importantly, it helps to solved mesophases that can not be identified using conventional SAXS on powder sample.

In this project, GISAXS experiments were mainly carried out at Station I16, Diamond Light Source (UK). The sketched set-up of GISAXS was shown in Figure 2.5a while photos of the real experimental set-up are shown in Figure 2.5b and 2.5c. The sample was placed on top of the sample holder, the temperature of which can be controlled remotely out of the experimental hutch. A helium chamber is placed between sample and detector to reduce background noises from air scattering. A lead foil strip was placed on the back of the helium chamber, used as the beamstop to block the primary as well as reflected beams, protecting the detector from damage. A 2D Pilatus-2M detector (Dectris) was used to record the scattering patterns.

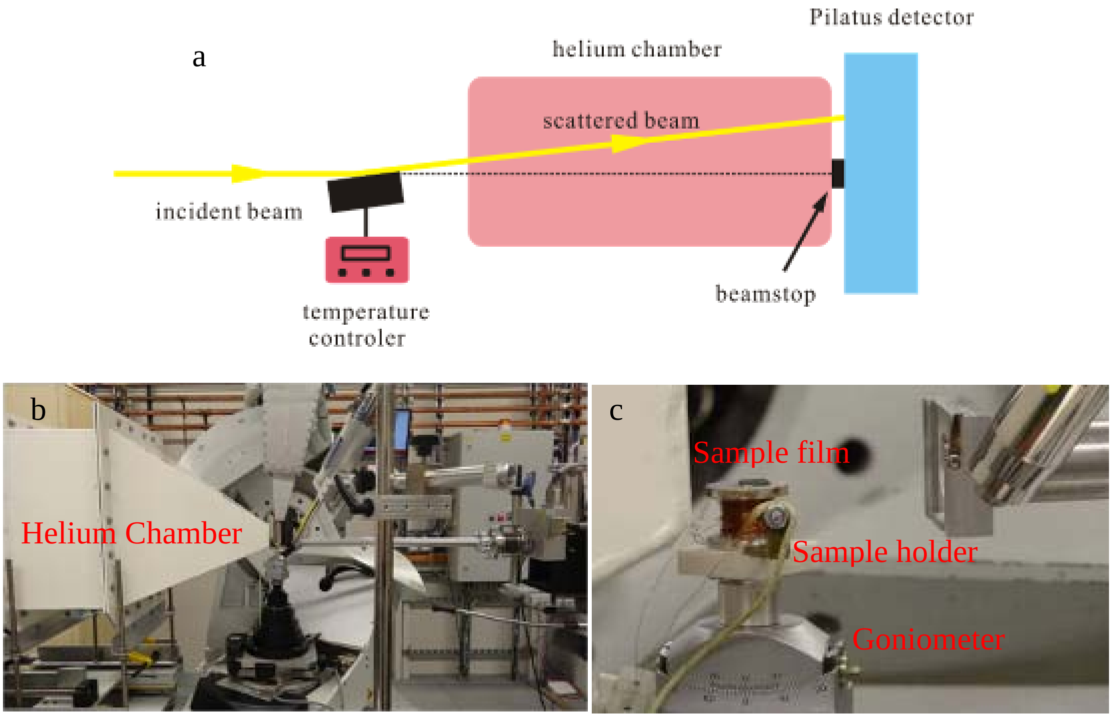

Figure 2.5 The GISAXS experimental setup at Station I16, Diamond Light Source. a) Sketch of the GISAXS setup; b) Real experimental set-up; c) A zoom-in photograph of the sample holder for the GISAXS experiment.

To prepare the thin film samples, firstly a silicon wafer substrate was cleaned by acetone then washed with distilled water before it is dried, often by using a hotstage. When the sample is prepared from melt, the sample was put on top of the substrate and heated up to melt to form the thin film, then the molten sample is spread by pressing with a second silicon wafer substrate before separation of the two wafers. Thin films can be prepared from solution as well, by drop casting or spinning coating.

2.3 Polarized Optical Microscopy

Polarized optical microscopy is a widely used technique to help study liquid crystals, and to help determine the phase transition temperatures and structures. Polarized optical microscopy can help us determine the type of mesophase based on their typical optical textures[4]. The schematic diagram and a picture of the polarized optical microscope (Olympus BX-50) used in this project are shown in Figure 2.6.

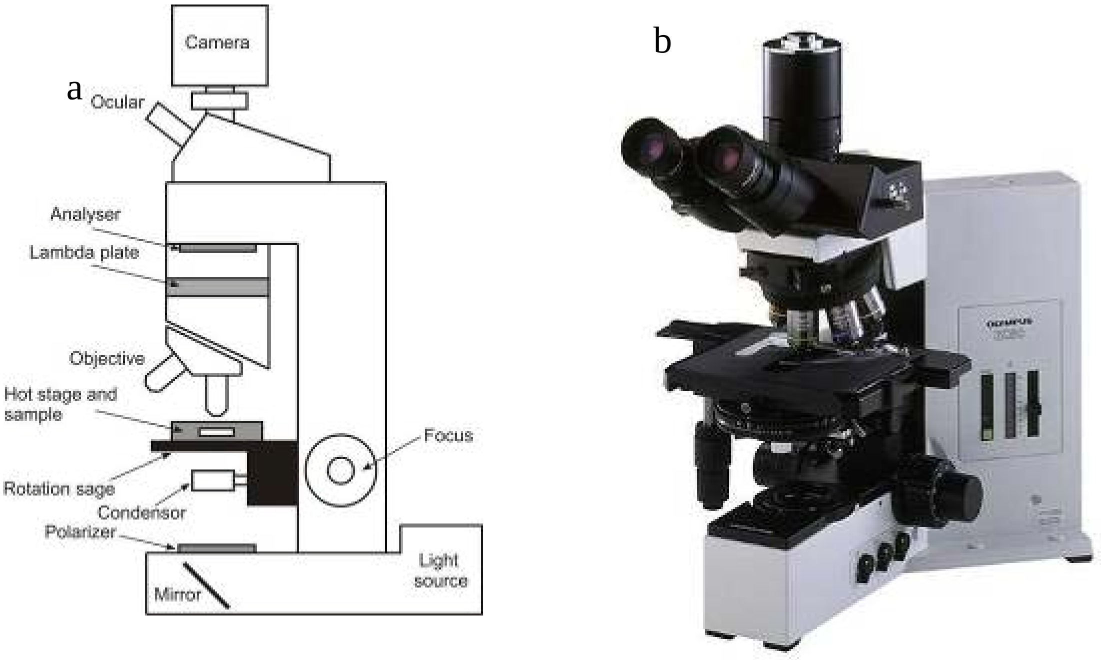

Figure 2.6 a) Schematic diagram showing the main components of a polarized optical microscope. b) Photograph of the Olympus BX-50 polarized optical microscope used in this project.

Light cannot pass through a pair of crossed polarizers. But if optically anisotropic samples are placed in between the crossed polarizer and analyzer, polarization condition of light will be changed by the sample and light will pass through. In the liquid crystalline state, the anisotropy of macroscopic physical properties is due to the orientational order of anisotropic molecules (rod-like or disk-like mesogens). And the index of refraction is dependent on the polarization direction of the incident beam. Consequently different orientational order of the liquid crystal results in different textures under polarized optical microscope. Some of these textures are so typical of a particular kind of LC phase that they can be used to identify them.

To be more precise, for many objects, such as glass and water, only one refraction index would exist as they are isotropic. However, anisotropic materials such as liquid crystals could possess two refraction indexes n_o (for so called ordinary ray) and n_e (extraordinary ray), respectively, which means that light would travel at different velocities depending on its direction of polarization. This phenomenon is called birefringence or double reflection as shown in Figure 2.7[4].

Then the retardation δ, or the phase difference between ordinary and extraordinary rays, is defined as[29]:

$$\delta = \frac{2\pi}{\lambda}(n_e - n_o)d \tag{2.20}$$

Where λ is the wavelength of incident light beam and d is thickness of the medium.

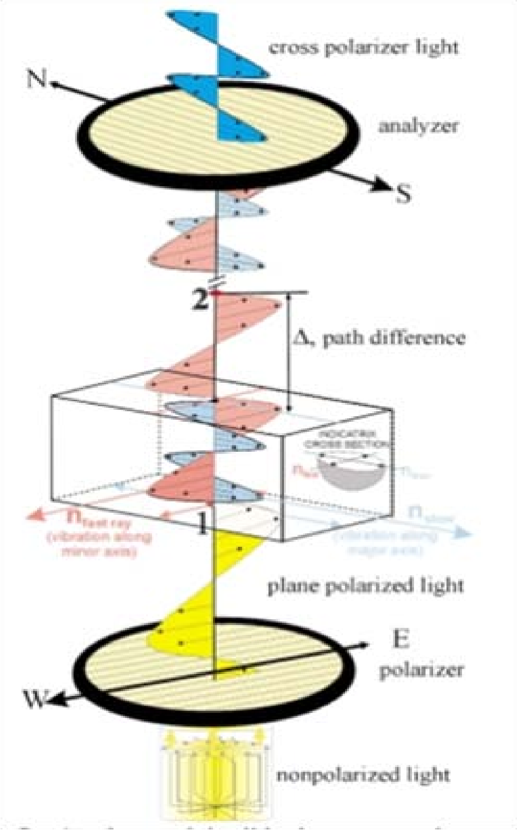

Figure 2.7 Interaction of polarized light with an anisotropic crystal.[34]

When the ordinary and extraordinary refracted beams travel through birefringent object, they would still keep vibrating at right angles with respect of each other, but the fraction that pass through the analyzer will change with the retardation angle. The measured intensity *I* after travelling through the birefringent materials is:

$$I = I_0 \sin^2 2\theta \sin^2 \frac{\delta}{2} \tag{2.21}$$

Where I_0 is the intensity of light passing the polarizer, θ is the angle between the polarizer and the optical axis of anisotropic material, δ is the retardation. Since the intensity I is dependent on the angle θ, if the sample is rotated, the brightness would change accordingly. The Michel-Levy chart provided in Figure 2.8 is usually used to investigate the colours seen in birefrigent materials quantitatively related to retardation, thickness and birefringence of the sample.

In order to control the background illumination and determine the orientation of the molecules in liquid crystalline phase, a retardation plate was often introduced to help interpret liquid crystalline textures by examining the slow and fast axis that light beam travels through the sample. A retardation plate is made up of optically anisotropic objects such as quartz and mica. Usually the direction of the retardation plate is northeast-southwest, which is marked as “slow”. In this project, we mainly use the 1-λ retardation plate to provide one full-wavelength retardation because the first order area in the chart is the most sensitive. Slightly difference would cause the colour to shift dramatically.

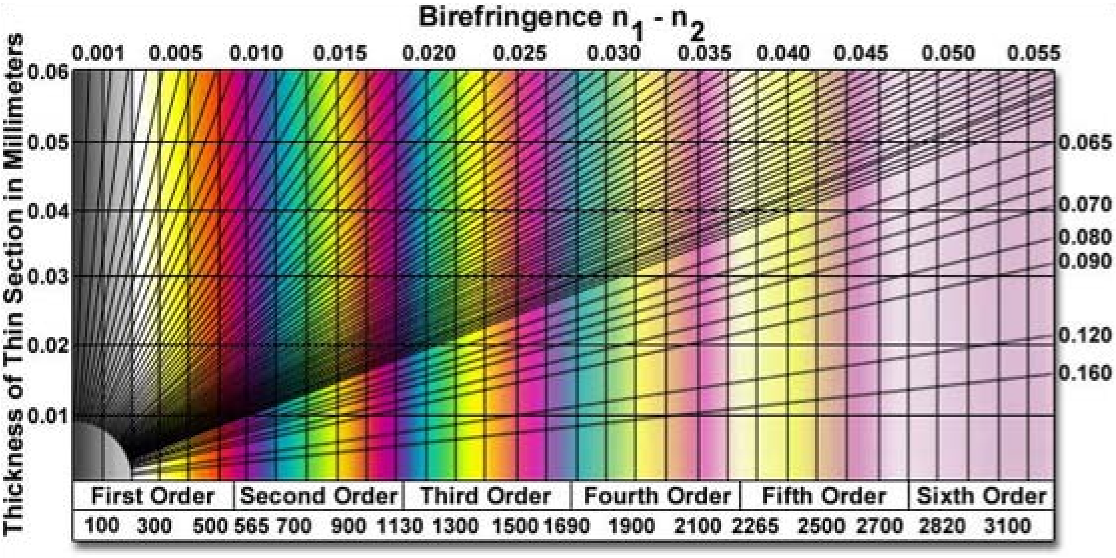

Figure 2.8 The interference colour chart.[35]

If the slow axis of the λ -plate is parallel to the slow direction of the sample, one additional full-wavelength retardation would be added up in this slow axis. Therefore, the first-order interference colour grey would present blue. Otherwise, if the slow axis is parallel to the fast direction of the sample, the initial fast wave would be slowed down and the interference colour may become first-order yellow. The fast and slow axis of the sample are corresponding to directions perpendicular and parallel to that of aromatic cores respectively. Therefore, on the basis of the observed interference colour, more details on the molecular arrangement in the liquid crystal phase can be retrieved.

2.4 Differential Scanning Calorimetry

Differential Scanning Calorimetry (DSC) is a technique which is used to measure the amount of heat needed to heat up or cool down a sample in reference to the temperature. It is a very powerful method to study phase transitions, to determine the thermodynamic quantities such as heat capacities and transition temperatures.

A DSC instrument is usually composed of two microcalorimeters, one for the sample and the other for the reference which is normally an empty pan. When the sample undergoes a phase transition, more or less heat ΔQ per time unit dt will need to flow to the sample in comparison to the reference, depending on whether the transition is exothermic or endothermic, in order to maintain the sample and reference at the same temperature. The DSC here will measure the quantity of the temporal change $d(\Delta Q) / dt$ of the sample as a function of the temperature.

In this project, the DSC measurements were carried out using a Perkin – Elmer Pyris 6 DSC machine, with a heating/ cooling rate of 5 °C/min under nitrogen atmosphere.

2.5 Analysis Procedure

2.5.1 Determination of Liquid Crystal Structures

To determine the structure of a liquid crystalline phase, several steps are included. Firstly, the *d*-spacings of the diffraction peaks need measuring. Based on the square ration of the *q*-values, the scattering peaks could be indexed, i.e. to determine for each peak its Miller indices (*hkl*). A combination of SAXS and GISAXS experimental results are often helpful. For example, the *d*-spacings of reflection index (*hkl*) for orthorhombic lattice could be written as,

$$\frac{1}{d^2} = \frac{h^2}{a^2} + \frac{k^2}{b^2} + \frac{l^2}{c^2} \qquad (2.22)$$

Where *a*, *b* and *c* are the lattice parameters for the unit cell and (*hkl*) are the miller indices of the lattice.

For orthorhombic lattice, $a \neq b \neq c$ and $\alpha = \beta = \gamma = 90°$. The relative ratio of reciprocal *d*-spacings would give an unambiguous identification on the lattice. Some typical mesophases with different symmetries in liquid crystals with relative *q*-values compared with the fundamental q^* are list in Table 3.1

Table 2.1 Theoretical ratios q/q* for Bragg reflections from various structures

Mesophase	Ratios q/q^*
Lamellar phase	1: 2: 3: 4: 5: 6…
Square Columnar phase	$1: 2^{1/2}: 4^{1/2}: 5^{1/2}: 8^{1/2}: 9^{1/2}$…
Hexagonal Columnar phase	$1: 3^{1/2}: 4^{1/2}: 7^{1/2}: 9^{1/2}: 12^{1/2}$…
Cubic bcc phase	$1: 2^{1/2}: 3^{1/2}: 4^{1/2}: 5^{1/2}: 6^{1/2}$…
Cubic fcc phase	$3^{1/2}: 4^{1/2}: 8^{1/2}: 11^{1/2}: 12^{1/2}: 16^{1/2}$…

After measuring the experimental *q*-values of diffraction peaks obtained from experimental diffraction patterns, simple structures as listed in Table 2 can be identified easily by comparing the experimental ratios with the theoretical ones. For more complex structures GISAXS patterns on oriented thin films will be helpful. After indexing of the diffraction peaks, the unit cell parameters can be determined and space group can be identified based on the general and special reflections rules (systematic absences) which could be found in the *International Tables for Crystallography*.[36]

After determining the unit cell, the numbers of molecules per unit cell based on density can be expressed as:

$$n_{\text{cell}}=V^*\ \rho^* N_A/\ M \tag{2.23}$$

Where V is unit cell volume, ρ is the density, N_A is the Avogadro constant and M is the molar mass of the molecule.

2.5.2 Reconstruction of Electron Density Map

After obtaining the structure information, next step is to determine the arrangement of molecules in unit cell by reconstruction of the electron density map using the measured diffraction intensities. Diffraction intensities of each observed peak can be acquired by fitting 1-D power diffraction spectra with Origin^{TM} software, which is often used to integrate intensity and resolve overlapped peaks. To minimize the background effect contributed by the capillary itself, the diffraction pattern of the empty capillary is recorded for subtraction of background.

The electron density $\rho(\vec{r})$ in any periodic structure can be written as the inverse Fourier transform the structure factor $F(hkl)$ as follows[4]:

$$\rho(x,y,z)=\sum_{h,k,l}\left|F(h,k,l)\right|\exp[-i2\pi(hx+ky+lz-\phi_{h,k,l})] \qquad (2.24)$$

Where $\phi_{h,k,l}$ is the phase angle of the structure factor. If a crystal is with a centre of symmetry at the origin, then the equation must meet the condition that the electron density $\rho(x,y,z)$ equals $\rho(-x,-y,-z)$. So the phase angle $\phi_{h,k,l}$ should only be 0 or π and the structure factor of any give *(h,k,l)* reflection is always real. As a result, the equation could be simplified as[4]:

$$\rho(x,y,z)=\sum_{h,k,l}\left|F(h,k,l)\right|\cos[2\pi(hx+ky+lz-\phi_{h,k,l})] \qquad (2.25)$$

In this case, the phase angle $\phi_{h,k,l}$ should only be either 0 or π.

Another way to determine the phase is by theoretically calculating the form factors on the nanoparticles covered with mesogens. As the diffraction intensity is the product of the form factor $[F_{\mathrm{nano}}(q)]^2$ which is determined by the nanoparticles, and the structure factor *S(q),* determined by the structure lattice. Assuming the nanoparticles are spherical, then form factor $F_{\mathrm{nano}}(q)$ could be given by[37]:

$$F_{nano}(q)=3(\rho_{nano}-\rho_{org})V_{nano}[\sin(qR)-qR\cos(qR)]/(qR)^3 \qquad (2.26)$$

Where ρ_{nano} and ρ_{org} are the electron density of the nanoparticles and surrounded organic molecules, respectively. R is the radius of the nanoparticle.

A Debye- Waller factor is also introduced to take the thermal displacement of nanoparticles from mean positions into consideration. As a result, the theoretical calculated intensity could be given as:

$$I(q) = M(q)S(q)\exp(-<u^2> q^2/3)[F_{nano}(q)]^3 \qquad (2.27)$$

Where $<u^2>$ is the mean square displacement of the nanoparticles and *M(q)* is the multiplicity of each reflection.

2.5.3 Molecular Modelling and Dynamics Simulation

Based on the reconstructed electron density map and molecular structure, the final step is to propose a structure model to fit the arrangement of molecules in each mesophase. Modelling and molecular dynamic simulation is carried out by Materials studio (Accelrys) software, which specializes in computational chemistry and molecular simulation. The whole process includes several steps as follows.

First of all, a crystal structure is built with experimental unit cell parameters. Based on the electron density map, molecules are arranged within the crystal in correspondence to the symmetry of the unit cell. Next energy minimization and geometry optimization are carried out to minimize the strain energy of molecules by locally adjusting the atomic positions. The final step is dynamics simulation, with repeated heating and cooling circles, to allow larger scale rearrangement of molecules, to obtain better molecular packing, and to check the stability of the structural model proposed.

Chapter 3 Gold Nanoparticles Covered with Hemi-Phasmids

This chapter studies the self-assembly of gold nanoparticles covered with hemi-phasmidic molecules. For comparison, the self-assembly of dimers of the Hemi-phasmids, as well as silsesquioxane cages covered with hemi-phasmids, are examined as well. 2-D ordered structures have been observed in such systems, investigated by Small-angle X-ray Scattering, Grazing Incidence Small-angle X-ray Scattering and Polarized Optical Microscopy. The results are presented in the following sections for hemi-phasmidic dimmers, silsesquioxane cages, and gold particles respectively.

3.1 Hemiphasmidic dimer

3.1.1 Molecular structure

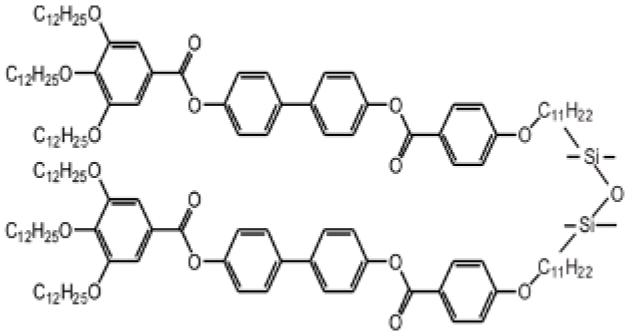

Figure 3.1 Molecular structure of hemiphasmidic dimer (Appreciate the samples provided by Prof. Georg H. Mehl's group in the University of Hull).

As shown in Figure 3.1, a hemiphasmidic dimer molecule is composed of two hemiphasmids. The rigid part of the hemiphadmid molecule contains four benzene rings linearly connected via two ester groups, while the flexible hydrocarbon parts include three terminal ends for each hemi-phasmid and the spacer between them. The combination of the rigidity of the core, and the mobility provided by the flexible end groups, are the driving force for self-assembly.

3.1.2 DSC results and discussions

Figure 3.2 presents the DSC traces of the first and second heating and cooling scans of the hemiphasmidic dimer. On the first heating scan, the hemiphasmidic dimer exhibited crystalline phase (normally associated with a higher melting enthalpy), which changed at 43 °C into a mesophase (columnar hexagonal, details see next section on X-ray diffraction experiments). The mesophase underwent isotropization at 55 °C. The main difference between the first and second heating scan is the lower enthalpy associated with the transition from the crystalline state to the mesophase in the second heating scan. That could be explained because in the first heating scan, the hemiphasmidic dimer crystallized from the solution, while in the second in cooling from the melt. The cooling scan from the isotropic phase shows an isotropic-mesophase transition at 56 °C. It is obvious that the formation of the crystalline phase of hemiphasmidic dimer is controlled by kinetics[6] and this was confirmed by X-ray diffraciton experiment: the crystalline phase reappear after longstanding at room temperature.

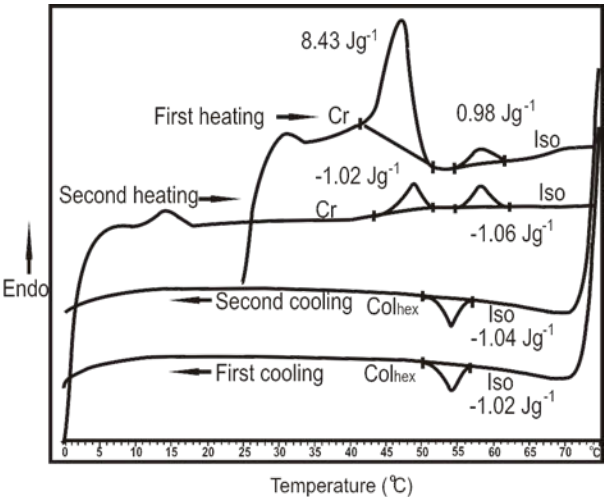

Figure 3.2 DSC scans of the hemiphasmidic dimer (Appreciate the DSC work provided by Prof. Georg H. Mehl's group in the University of Hull).

3.1.3 SAXS and GISAXS results and discussions

Figure 3.3a presents the SAXS diffractograms that were recorded during heating from room temperature to isotropic (60°C) and then quickly cooled (10 °C/min) to 35 °C. After long standing at room temperature (overnight), the same sequence was recorded again. A phase sequence, including crystalline I phase (as received), crystalline II phase (35 °C), the columnar hexagonal phase (45 °C) and isotropic phase (above

50 °C) in heating, and the hexagonal phase (35°C) when cooled from isotropic to 35 °C, is observed. The hexagonal nature of the mesophase is confirmed by GISAXS experiment, on a thin film sample prepared from melt, recorded at 37 °C. The hemiphasmidic dimer crystallized, and the crystal II phase was regained, on long standing at room temperature. This indicates that the hexagonal phase of hemiphasmidic dimer was metastable at temperatures below ~40°C. The same phase sequence, first to the mesophase, followed by isotropic on heating, and the formation of the mesophase on cooling, is observed on second heating/cooling scan as on the first one.

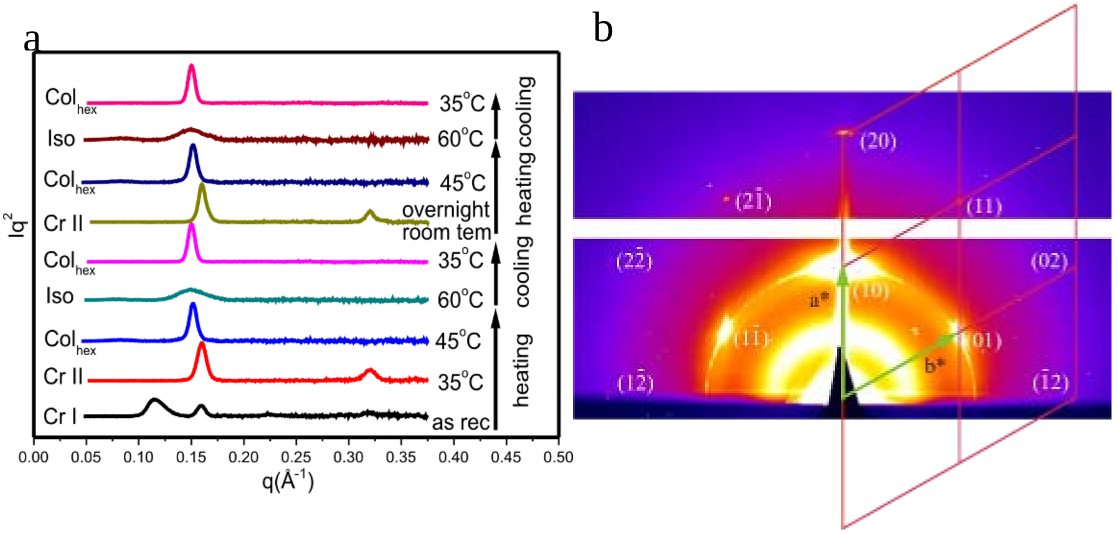

Figure 3.3 a) SAXS diffractograms of the hemiphasmidic dimer. b) GISAX pattern of the columnar hexagonal phase of hemiphasmidic dimer, recorded at 37 °C, with reciprocal lattice and indices for the observed reflections overlaid on top.

From room temperature to 50 °C, sharp diffraction peaks were observed in Small angle X-ray scattering (SAXS) experiment and birefringence could be observed under polarized microscope. Above 50 °C, sharp peaks disappeared and only diffuse peaks were observed, indicating the formation of isotropic phase which was confirmed by the lack of birefringence.

The GISAXS pattern, recorded at 37 °C of a surface aligned sample (quickly cooled from isotropic), is shown in Figure 3.3b and clearly presented a 2D lattice with hexagonal symmetry with plane group *p6mm*. The lattice parameter *a* is calculated to be 47.9 Å. The indices, and experimental and calculated *d*-spacings of the observed reflection of the $\mathrm{Col_{hex}}$ phase are listed in Table 3.1.

Based on the equation 2.23, the unit cell volume could be obtained from the lattice parameter a_{hex}=47.9 Å, and assume a height of c=4.5 Å corresponding to the average stacking distance along the column direction: V_{cell}=8942 $Å^3$. Assumed density ρ=1.0g/ml so for the hemiphasmidic dimer ($C_{150}H_{234}O_{17}Si_2$), the number of molecules in a unit cell can be estimated to be 2.3. As the molecular length (L) of hemiphasmidic dimer in their most extended conformation, spanning between the ends of two alkyl chains at opposite sides of the molecule, is 114.3 Å. As $2a < L < 3a$, the hemiphasmidic dimers must fold back to be accommodated in the unit cell.

Table 3.1 Experimental and calculated d-spacings for the $\mathrm{Col_{hex}}$ phase of hemiphasmidic dimer recorded at 37 °C

(hk)	$D_{obs.}$-spacing/ Å	$D_{cal.}$-spacing/ Å	Intensity	Multiplicity	Angle
(10)	41.4	41.5	1865.3	6	0
(11)	24.0	24.0	22.53	6	0
(20)	20.8	20.7	53.9	6	0
a = 47.9 Å					

3.1.4 POM results and discussions

The orientation of the π-conjugated aromatic quaterphenyl cores was deduced from the colours of the fan-like textures in the polarized optical microscopy taken with a λ-plate retarder (Figure 3.4b). The yellow and blue colours indicates that the axis of high refractive index is radial rather than tangential. Since the columns are normally tangential in the fan-like textures for columnar hexagonal phase (the bending direction perpendicular to the column axis), and the high-index axis is known to be parallel to the quaterphenyl long axis, it follows that the quaterphenyls are more or less perpendicular to the column long axis.

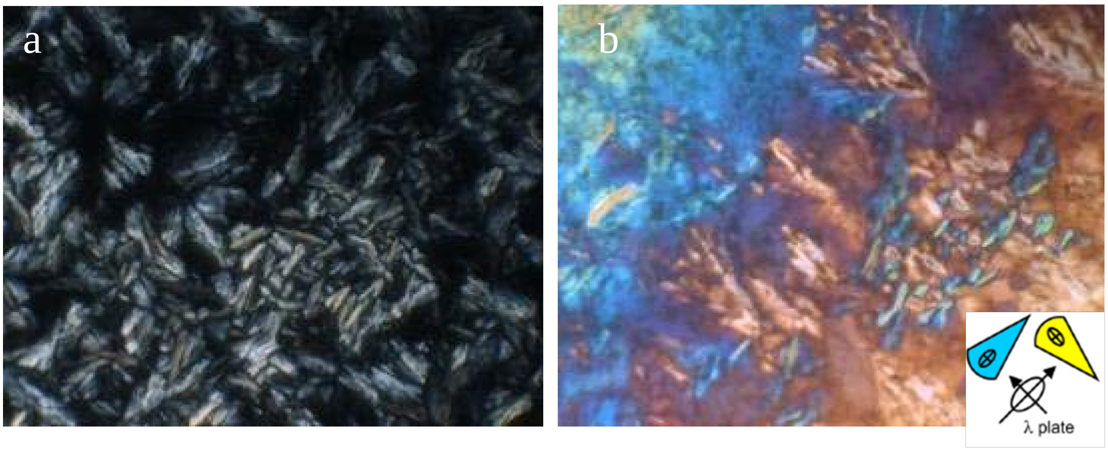

Figure 3.4 a) Texture of the columnar hexagonal phase of the hemi-phasmidic dimer under crossed polarizers recorded at 50 °C. b) The same phase recorded at the same temperature with λ-plate retarder. The indicatrix orientation in the λ-plate and in the two types of fans is shown in the inset.

3.1.5 Reconstruction of electron density map and proposed model

Diffraction intensities measured by Origin^{TM} software from powder diffraction pattern were used to reconstruct the electron density map (Figure 3.5) of this columnar hexagonal phase. Based on the integrated intensity from GISAXS pattern shown in Table 3.1, electron density map is drawn as shown in Figure 3.5. In the map, the circular high electron density areas, purple and blue, were located at the corner of hexagonal lattice surrounded by the lowest electron density part, red area.

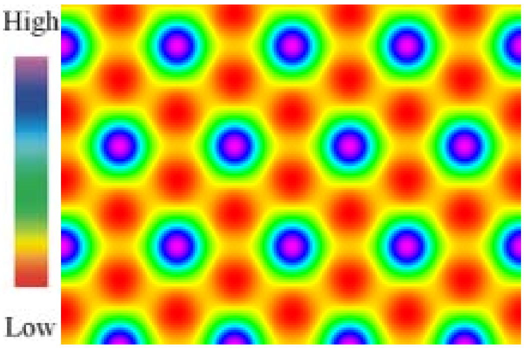

Figure 3.5 The electron density map of the Col$_{hex}$/*p6mm* phase of hemiphasmidic dimer

Based on the calculation of electron density of each part of the molecule listed in Table 3.2, the rigid aromatic core has the highest electron density so they should lie at the corners of the hexagonal lattice, while the red area should be taken up the alkyl end groups and spacers.

Table 3.2 Electron density of each part of the molecule

Name	Volume (A^3)	Numbers of Electrons	Electron Density (e^-/nm^3)
Alkyl Chain	1387.2	582	420
Aromatic Core	883.6	456	516
Spacer	507.09	216	426

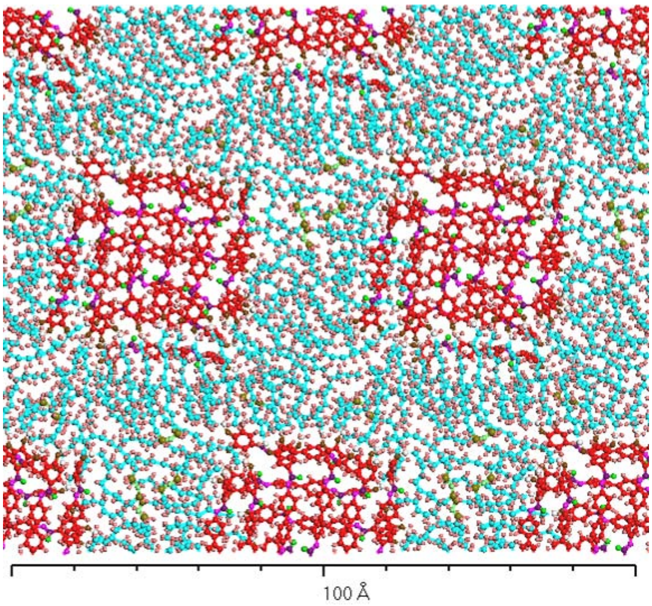

Figure 3.6 Snapshot of a molecular dynamics simulation, colour coding is: red and purple = aromatic cores; Blue, pink and green = alkyl chain and spacers

Based on the unit cell parameters, molecules numbers and the direction of the rigid cores of molecules in hexagonal lattice, moleculear models of the columnar hexagonal phase has been constructed, and molecular dynamics simulation carried out using Materials Studio (Accelrys^{TM}). A snapshot of the molecular model during dynamics simulation is shown in Figure 3.6, which was modelled by using Materials Studio. The simulation confirms that reasonable space filling and separation were achieved in the proposed structure.

3.2 Silsesquioxane Cages Covered with Hemi-Phasmids

3.2.1 Molecular structure

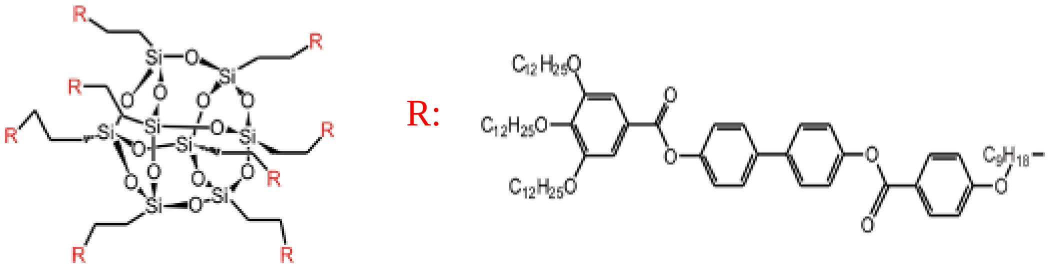

Figure 3.7 Molecular structure of silsesquioxane cages and attached hemiphasmidic mesogen (Appreciate the samples provided by Prof. Georg H. Mehl's group in the University of Hull).

3.2.2 SAXS and GISAXS results and discussions

Figure 3.8a presents the SAXS diffractograms which were recorded during heating from room temperature to 120 °C and cooling to 55 °C afterwards. Only diffuse peaks due to short-range order were observed in SAXS, as well as in GISAXS patterns as shown in Figure 3.8b. Lack of birefringence under polarized optical microscopy confirmed the phase being isotropic. There is also no phase transition observed in DSC traces between 30 °C and 130 °C, both on heating and cooling. These results showed that, no long-range order, or any liquid crystalline phase could be obtained for this compound.

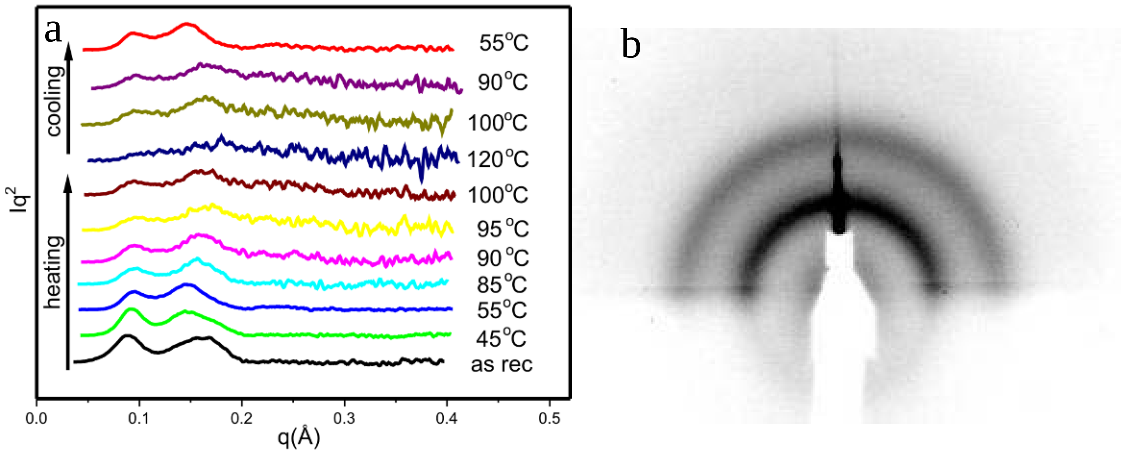

Figure 3.8 a) SAXS diffractograms of silsesquioxane cages covered with hemi-phasmidic mesogens. b) GISAX patterns of a thin film of silsesquioxane cages

covered with hemiphasmidic mesogens recorded at 80 °C after slow cooling (1 °C/min) from 120 °C.

3.3 Gold Nanoparticles Covered with Hemiphasmids

3.3.1 Molecular structure

The gold naoparticles were synthesized through a two-step method as discussed before. A schematic model of the gold nanoparticles covered with mesogenic ligands and alkyl co-ligands is shown in Figure 3.9.

In this model, the gold nanoparticles are located in the center surrounded by the ligands and coligands. The ligands, i.e. the hemi-phasmids, and the alkyl co-ligands, are end attached to the gold nanoparticle through a thiol group. The molar ratio of ligands/co-ligands, is found to be 1:1 on the basis of NMR experiment.

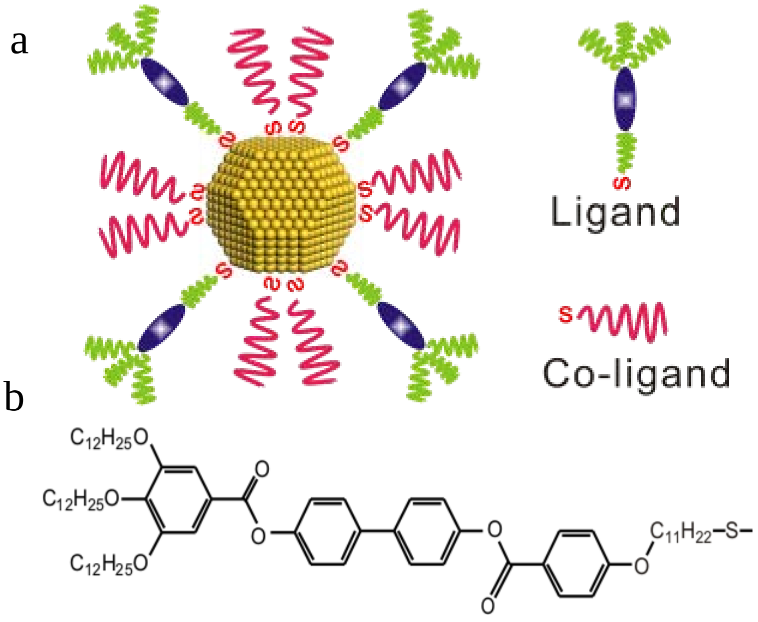

Gold nanoparticles:

(diameter 1.6-1.7nm)

Co-ligand: C_6H_{13}-S-

The molar ratio of ligand/co-ligand is 1:1

Ligand

Figure 3.9 a) Schematic model of gold nanoparticles covered with hemiligands and co-ligands. b) Molecular structure of the hemi-phasmid. (Appreciate the samples provided by Prof. Georg H. Mehl's group in the University of Hull).

3.3.2 SAXS and GISAXS results and discussions

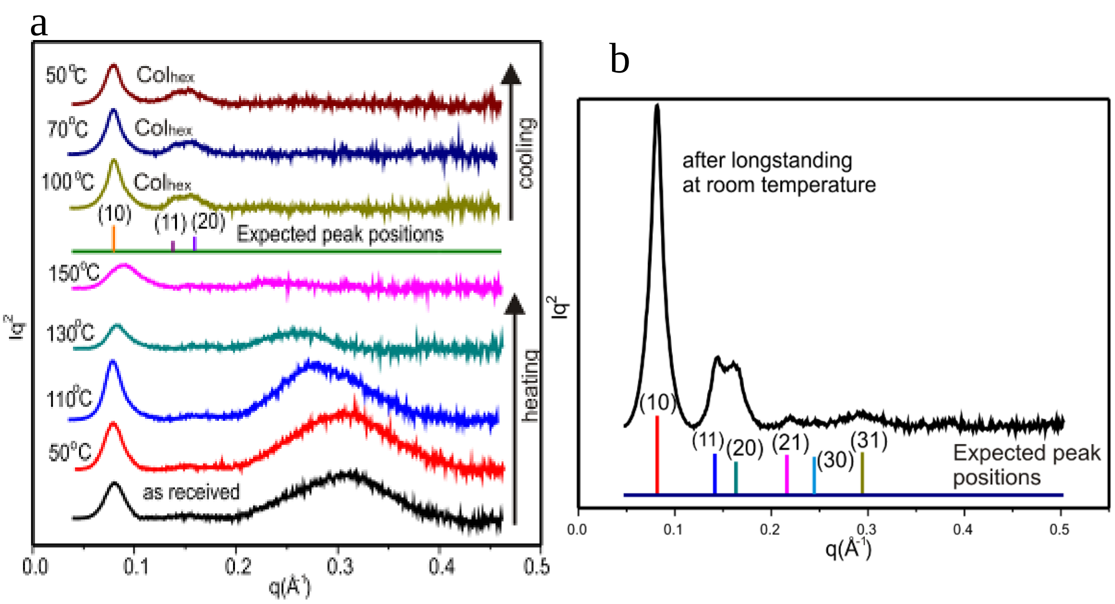

Figure 3.10 a) SAXS diffractograms of the gold nanoparticles covered with hemi-phasmidic mesogen. b) Experimental (top) and expected peaks positions (bottom) of SAXS powder diffractograms of the Col_{hex} phase of gold nanoparticle covered with hemi-phasimidic mesogens.

Figure 3.10a presents the SAXS diffractograms recorded during heating from room temperature to 150 °C and then cooling to 50 °C. In heating process, one broad peak (q range 0.2 – 0.4 $Å^{-1}$) disappeared gradually while the peak around 0.08 $Å^{-1}$ beomes sharper, before it broadens again when the compound becomes isotropic. This could be explained that with increasing temperature, mesogens got more freedom and mobility. And under the driving force provided by the parallel alignment of the anisometric mesogens and the free movement of the flexible chains, gold nanoparticles could gradually form long-range order on the mesoscale.

After cooling from isotropic phase, the diffraction pattern in the small-angle region was characterised by three Bragg reflections with a reciprocal spacing ration of $1:3^{1/2}:2$, which could be indexed as (10), (11) and (20) of a hexagonal lattice with plane group *p6mm*. After long standing at room temperature, the diffractogram (Figure 3.10b) shows even more diffraction peaks, all can be indexed on columnar hexagonal lattice with lattice parameter a_{hex} =88.9 Å. The observed and calculated *d*-spacings of diffraction peaks were compared in Table 3.3, and a good agreement between the two is achieved. The molecular length (*L*) of the hemi-phasmidic mesogen in their most extended conformation is 57.1 Å. Adding the diameter of nanoparticles 20 Å, the distance between two nanoparticles was 134.3 Å ($a < L < 2a$). This suggests some degree of interdigitation of the aliphatic chains of ligands attached to neighbouring nanoparticles in the unit cell.

To help confirm this indexing scheme, grazing incidence small angle X-ray scattering experiments were also carried out on an thin film sample prepared on silicon substrate. However, the thin film sample is found to be unoriented, so powder-like diffraction patterns are observed, even though good agreement on the *d*-spacings of diffraction peaks have been achieved between the SAXS and GISAXS results.

Table 3.3 Experimental and calculated d-spacings for the Col$_{hex}$ phase of gold nanoparticles covered with hemiphasmidic mesogens recorded at 37 °C.

	D-spacing (Å)		Intensity		Multiplicity	Phase angle
(hk)	Exp.	Calc. *p6mm* a = 88.9 Å	Exp	Model Dsphere= 22.8 Å ⍰ $\sqrt{\langle u^2 \rangle}$ =6.5Å Δ=15.5*		
(10)	77.3	77.0	100	100	6	0
(11)	44.0	44.5	10.3	19.8	6	0
(20)	38.9	38.5	15.9	6.2	6	0
(21)	28.7	29.1	0.8	1.9	12	
(31)	21.3	21.4	4.2	4.2	12	

$$^{*}\Delta = 100\left(\sum_i \left| I_i^{\exp} - I_i^{calc} \right|\right) / \left(\sum_i I_i^{\exp}\right).$$

3.3.3 Reconstruction of electron density map

Diffraction intensities, measured using Origin^{TM} software from powder diffraction pattern, were used to reconstruct the electron density map (Figure 3.11) of this columnar hexagonal phase. The first three peaks were used here to determine the electron density map based on the unit cell parameters and space group information. During this process, the multiplicities of different reflections were also taken into consideration as listed in Table 3.3. How to choose the right phase was detailed in Appendix. In the map, the circular high electron density areas, purple and dark blue, are located at the corners of the hexagonal lattice, surrounded by the low electron density area, red and green parts.

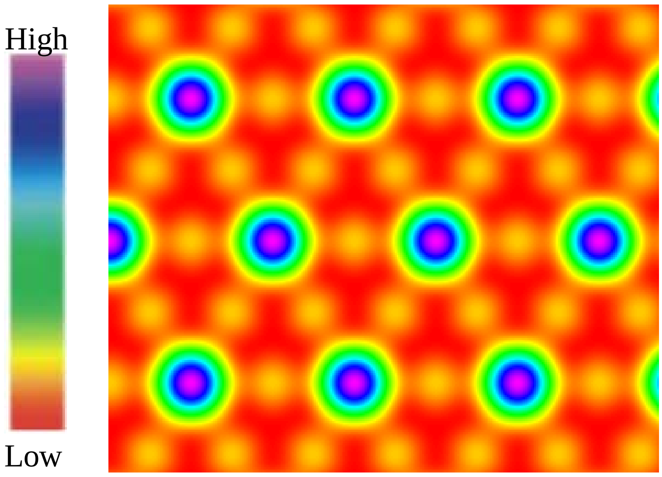

Figure 3.11 Electron density map of gold nanoparticles covered with hemiphadmids based on the integrated intensities of first three peaks

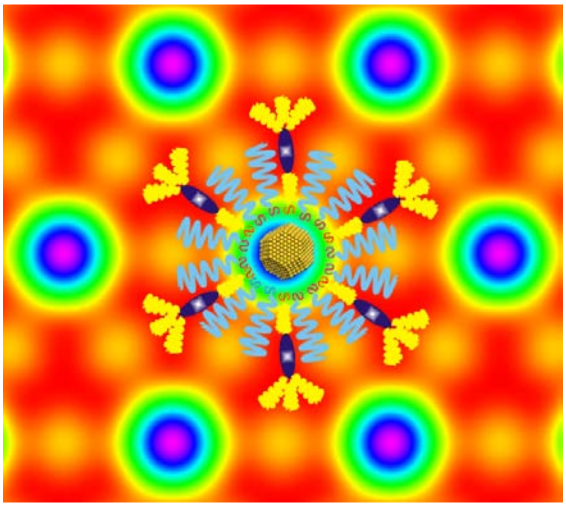

Figure 3.12 Proposed model of molecule arrangement based on the electron density map.

Based on the calculation of electron density of each part of the molecule listed in Table 3.4, the gold nanoparticle had the highest electron density (10 times higher than organic parts) so it’s reasonable to assume the gold nanoparticles would lay in the corner of the hexagonal lattice. While the low electron density part, red and green areas would be taken up by the alkyl chains at the terminal ends as they contained the largest volume in correspondence. Based on the electron density map, the proposed model is drawn on the top.

Table 3.4 Electron density of each part of the molecule

Name	Volume (A^3)	Numbers of Electrons	Electron Density (e/nm^3)
Gold nanoparticle	18.28	79	4322
alkyl chain ($C_{36}H_{78}$)	648	294	454
Aromatic core ($C_{26}H_{14}O_8$)	425	234	551
Spacer ($C_{11}H_{23}S$)	211	105	498

The size of the nanoparticles were determined by fitting the experimental diffraction intensities. In the latter, gold nanoparticles are assumed to be spherical with uniform high electron density inside, located in the centre surrounded by the organic molecules with uniform low electron density. This is justified by the calculated electron density listed in the Table 3.4, the electron density of gold nanoparticles is ten times larger than that of organic parts, that the minor changes in the organic parts can be safely ignored. The Debye- Walller factor was introduced to reflect the position fluctuations of gold nanoparticles from their mean positions. The best fit of the intensity simulation compared with experimental one was listed in Table 3.3. The diameter of the gold nanoparticles was best fit to be 22.8 Å and the mean square displacement of the gold nanoparticles $\sqrt{\langle u^2 \rangle}$ was calculated to be 6.5 Å.

The next step was to calculate the volume occupied by the gold nanoparticels as well as the surrounded organic parts. The gap between nanopaticles along the columnar axis should more or less determined by the length of the coligand, and according to results from reference[38] on a compound (AuL4C6) with C_6H_{13}-S, assuming the gap between the nanoparticles to be the same as 4.8 Å, hence the inter-particle distance can be estimated to be 27.6Å. So the unit cell volume could be obtained from the lattice parameter, a_{hex}=88.9 Å and the interparticle height of c=27.6Å, to be $V_{\text{cell}}=1.88\times 10^5$ Å^3. The volume of each Au atom was 17 Å^3 and the covered ligand and coligand volume were 1260 and 147 Å^3, respectively. Assuming that the density ρ was 0.9×10^3 kg/m^3 for the organic parts, the number of Au atoms in each nanoparticle was estimated to be 364 with a diameter of

22.8 Å. And the number of attached ligand and coligand was calculated to be 129, respectively as the ration between the two was 1:1. As listed in the Table 3.3, a good agreement between the experimental results and simulation was achieved.

3.4 Summay

In summary, three different hemi-phasmid-based systems have been studied and two different columnar hexagonal phases are observed, confirmed by SAXS, GISAXS, DSC and POM methods. The 2-D columnar hexagonal self-assembled arrangement of gold nanoparticles was accomplished with end-attached liquid crystalline molecules, i.e. hemi-phasmids. A columnar hexagonal (a= 88.9 Å) phase is found, the order of it improves by cooling slowly from the isotropic phase (above 100 °C). The new columnar hexagonal phase is different from that found in phasmidic dimer as the unit cell parameter is nearly twice of that in the dimer (a= 47.9 Å). No liquid crystal phase could be obtained for the silsesquioxane compound. The results also demonstrates that phasmidic molecules, in addtion to rod-like molecules, are capable of helping the self-assembly of nanoparticles.

Chapter 4 Self-assembly of 2,4-bis(4-dodecyloxy-benzylidene)cyclohexanone

4.1 Molecular structure

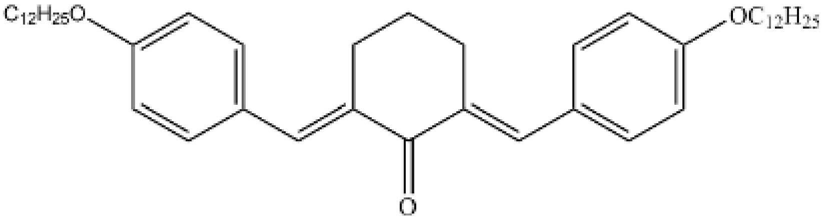

Figure 4.1 Molecular structure of DBCH (Appreciate the samples provided by Dr. Liliana Cseh's group in the Institute of Chemistry Timisoara).

2,4-bis(4-dodecyloxibenzilidene)cyclohexanone (DBCH, $C_{44}H_{66}O_3$) is a rod-like molecule composed of rigid part with two benzene rings linked by cyclohexane as the bridge and alkylchains at terminal ends. The molecular structure was shown in Figure 4.1. Instead of classical structures of "rod" shape, DBCH compounds still could develop liquid crystal behaviours. DBCH has angular ring systems, substituted by side chains, linking to cyclohexanone core via double bonds. The aromatic rings give the whole molecule the stability of direction.The substituted alkyl chains provide the fluidity. DBCH has also been found to undergo interesting change in its optical properties when exposed to Ultraviolet light, possibly due to change in its molecular configuration. Future work is needed to fully investigate such behaviours, but in this chapter we focus on the liquid crystal forming properties of the compound in its original form.

4.2 DSC results and discussions

Figure 4.2 shows the DSC traces of DBCH. As shown in Figure 4.2a, on heating of the as received sample (first heating scan), DBCH transformed from a crystalline phase (crystal-I), into a smectic mesophase (as determined by SAXS and polarized optical microscopy) at ~104°C, followed by an isotropization transition at 128.4 °C. On the subsequent cooling scan, DBCH showed first isotropic-smectic phase transition, then a transition to a new crystalline phase (crystal-II) at ~90°C, followed by another transition at ~74 °C into crystal I phase. The second heating scan was essentially the same as the first heating. In order to capture more clearly the phase transition from the crystal-II phase to the smectic phase, another experiment was carried out where the cooling scan was stopped at 80 °C followed by subsequent heating immediately (Figure 4.2b). In this case, only one phase transition peak appeared on heating at the crystal-II-smectic transition at 98 °C.

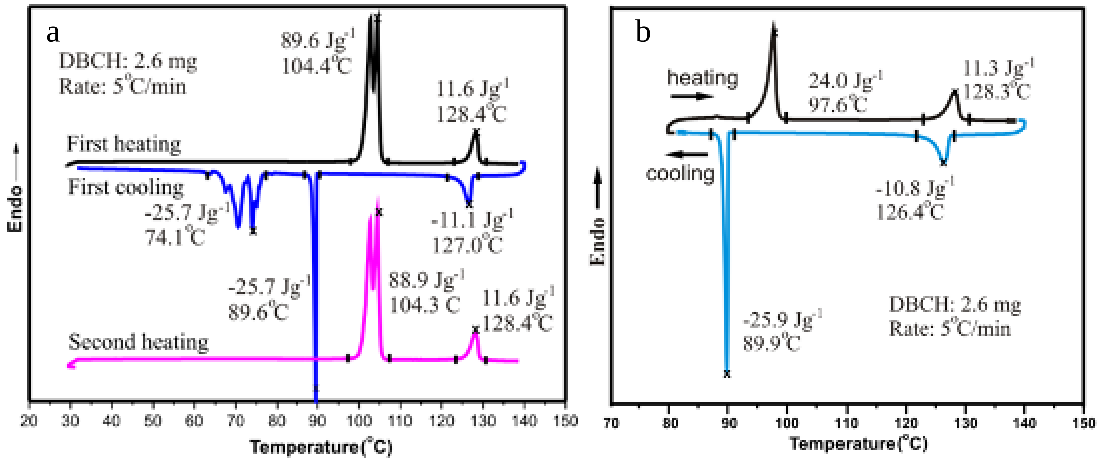

Figure 4.2 DSC thermal scans of DBCH with heating and cooling rate of 5 °C/min under nitrogen atmosphere

4.3 SAXS results and discussions

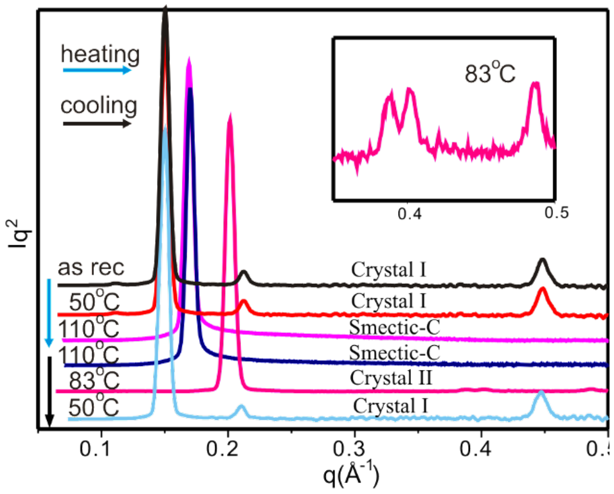

Figure 4.3 SAXS diffractograms of DBCH

Figure 4.3 presents the SAXS diffractograms of DBCH which were recorded during heating from room temperature up to 140 °C (isotropic) and then cooling to 50 °C. Several different phases, including crystal-I (50 °C), smectic phase (110 °C) and isotropic phase (above 130 °C) in heating, and smectic phase (110 °C), crystal-II phase (83 °C) and crystal-I phase (50 °C) in cooling, were observed.

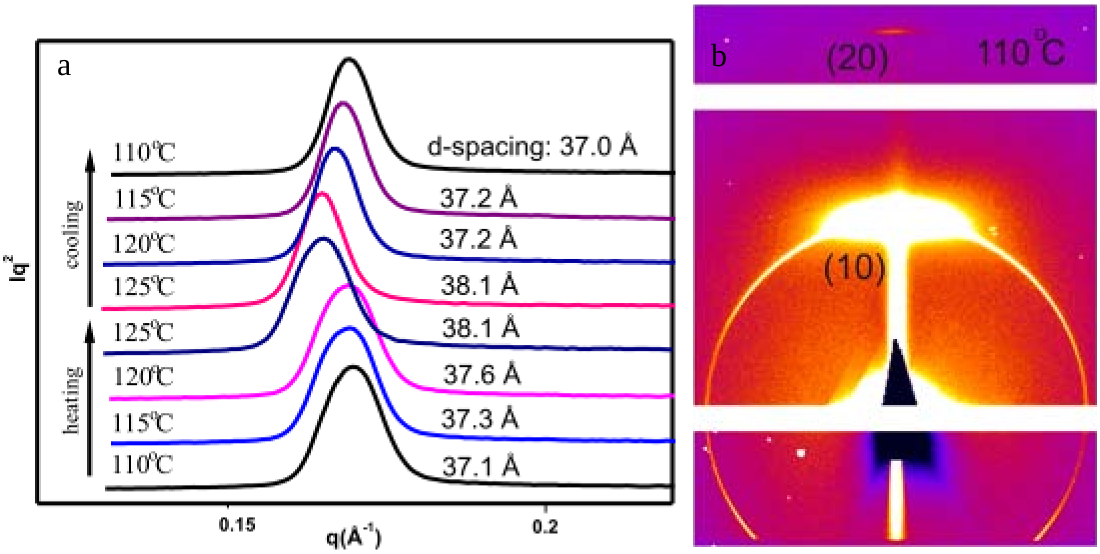

Figure 4.4 a) SAXS diffractograms of DBCH at temperature region of smectic phase b) GISAX pattern of smectic phase of DBCH recorded at 110 °C with reciprocal lattice and indices for the observed reflections

Only one diffraction peak is observed in the SAXS experiment for the mesophase in the temperature range between 100 °C and 125 °C (Figure 4.4a). However, using GISAXS on a thin film sample using synchrotron radiation source, a second order diffraction peak is also observed (Figure 4.4b), confirming the smectic nature of the mesophase. The orientational order of in the thin film sample is very high, as indicated by the also spot like diffraction peaks observed on the meridian. This also indicate that the normal of the smectic layers is perpendicular to the substrate.

Figure 4.4a also shows the change to the diffraction peak position in the temperature region of the smectic phase in response to changing temperature. The diffractograms were recorded every 5 degrees on heating and on cooling from isotropic. The *d*-spacing of the peak, which was in correspondence of the thickness of the smectic layer, increased as the temperature heated up and the vice versa. The layer thickness,

~ 37 to 38 Å is less than the length of the molecule at its most extended conformation (45 Å). The molecular length (L) of DBCH in their most extended conformation is calculated as 45 Å using molecular model (Materials Studio). These suggest that the phase being Smectic-*C* type, with the tilting angle decreasing with increasing temperature.

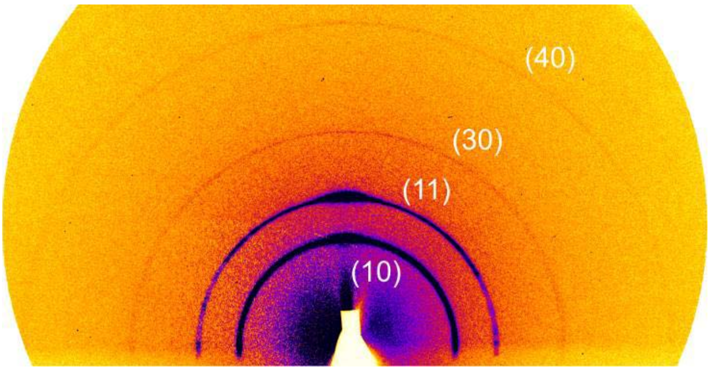

Figure 4.5 GISAX pattern of crystal-I phase of DBCH recorded at 50 °C

Table 4.1 Experimental and calculated d-spacings for the $\mathrm{Col}_{squ}/p4mm$ phase of DBCH recorded at 50 °C

(hk)	$d_{obs.}$-spacing (Å)	$d_{cal.}$-spacing (Å)	*Multiplicity*	*Intensity* (10^{-4})
(10)	42.0	42.0	4	371.4
(11)	29.8	29.7	4	13.9
(30)	14.0	14.0	4	43.4
(40)	10.5	10.5	4	35.2
a = 42.0 Å				

The GISAXS diffraction pattern of the crystal-I phase shown in Figure 4.5, recorded at 50 °C in cooling process. In the small-angle region it is characterized by four Bragg reflections, with a reciprocal spacing ration of 1: $2^{1/2}$: 3: 4. They can be indexed as (10), (11), (30) and (40) on a columnar square lattice with lattice parameters a = 42.0 Å. The indices, and experimental and calculated *d*-spacings of the observed reflections of the $\mathrm{Col}_{\mathrm{squ}}/p4mm$ phase were listed in Table 4.1. The index of the crystal-I is only partial: it should be 3-D, but we have only 2-D indexing for the small angle region. We are not so sure about the square symmetry either.

GISAXS/GIWAXS on oriented thin films have been carried out recently, and further work is need to elucidate the structures of the crystal-I and crystal-II phases.

4.4 POM results and discussions

As shown in Figure 4.6a, a thicker film of DBCH at 110 °C showed typical focal conic structure which can be attribute to a smectic structure. More interestingly, when the film is thin, schlieren texture could be observed as shown in Figure 4.6b (the black area is due to the bubbles). Such behaviour has been observed for homeotropically (the smectic normal is perpendicular to the surface) aligned Smectic-C phases, due to the orientation variation of the tilt direction. In fact, the homeotropic alignment of thin film on the silicon substrate is confirmed by the GISAXS results showing in Figure 4.4b.

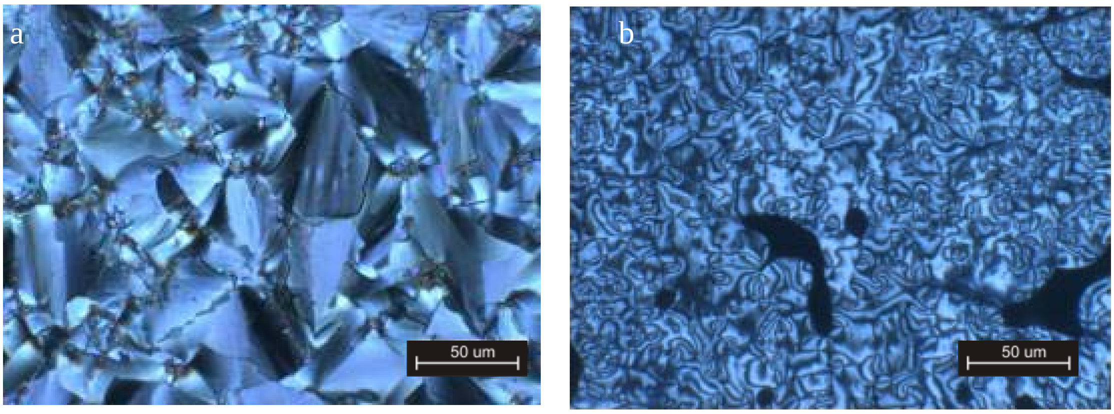

Figure 4.6 Textures of the phase of DBCH recorded under crossed polarizers cooled from isotropic phase at 140 °C to 110 °C with the cooling rate of 1 °C/min a) thick film b) thin film.

In summary, two different crystalline states, and a Smectic-*C* phase (*a*=36.9-38.1 Å depending on temperature) was observed for DBCH.

Chapter 5 Dendronized Cadmium-Sulphide Nanoparticles

5.1 Molecular structure

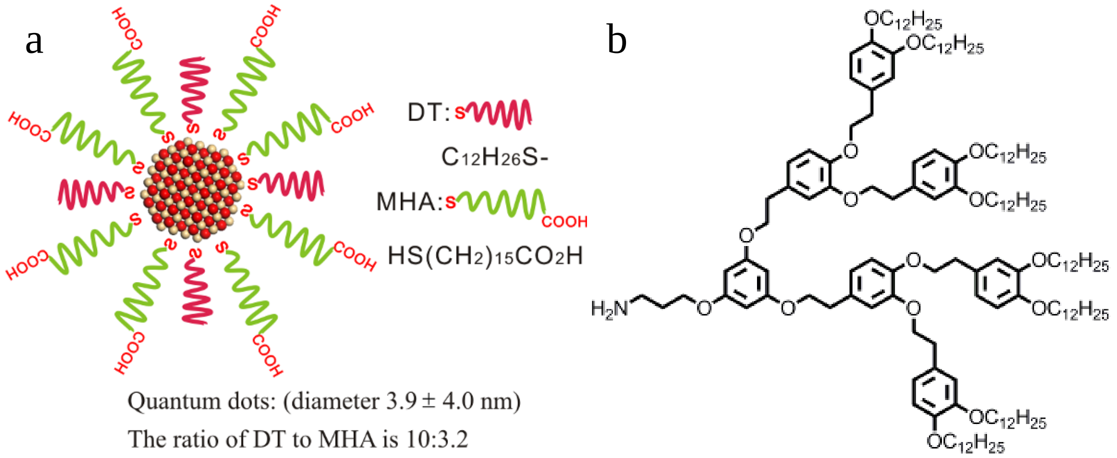

Figure 5.1 a) Schematic model of CdS quantum dots. b) Chemical molecular structure of attached dendrons (Appreciate the samples provided by Prof. Atsushi Muramatsu's group in the Tohoku University).

Semiconductor nanoparticles, which are known as quantum dots, have attracted great attention due to the fascinating optical properties such as size-dependent, tunable adsoption and emission.[23] Besides, period arrangement of quantum dots has potential in applications for novel nano-electronic device based on interaction of electronic charge and spin within and between quantum dots materials.[30] The simple cubic packing of gold nanoparticles with dendrimeric outer corona has been achieved in our group. [32] Here we report our study on a similar dendronized CdS quantum dots. Figure 5.1a shows the molecular structure of Cadmium Sulphide (CdS) quantum dots, covered by 12-dodecanethiol (DT) and 16-mercapto hexadecanoic acid (MHA) molecules (constituents of the inner corona). At the second step, the dendrons shown in Figure 5.1b, were attached as the outer corona via amidation to the carboxylic groups at the surface of the inner aliphatic corona functionalized nanoparticles.

The dendrons themselves have been found to form the liquid quasi-crystal phase[39] of spherical micelles of diameter ~ 9.8 nm.[36] In this chapter, we were mainly interested in investigating the arrangement of the nanoparticles CdS under the influence of the attached dendrons.

5.2 GISAXS results and discussions

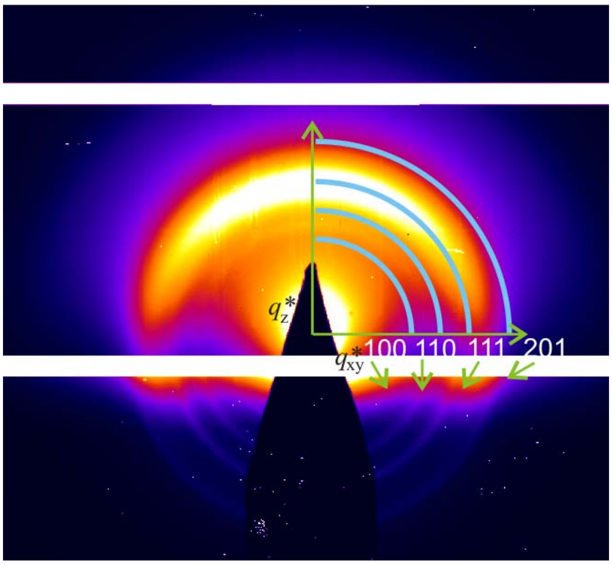

Figure 5.2 GISAXS pattern of cubic structure of quantum dots CdS covered with dendrons prepared from chloroform solvent annealed at 150˚ C in vacuum oven for 6 hours.

First test was carried out by SAXS on powder sample, but only broad peaks were observed. So we move on to check GISAXS on thin film sample. The thin film of quantum dots CdS covered with dendrons on silicon wafer was prepared from chloroform solvent annealed at 150 °C in vacuum oven for 6 hours. The GISAXS pattern, of the thin film sample as shown in Figure 5.2, in the small-angle region was characterized by four Bragg reflections. The diffraction intensity is so strong that it would penetrate the subtrate and be seen under the horizon. And due to less interference from background caused by the reflected beam, peaks below horizon can be seen clearer. With a reciprocal spacing ration of 1: $2^{1/2}$: $3^{1/2}$: $5^{1/2}$, the four peaks could be either indexed as the (100), (110), (111) and (210) diffraction peaks of a simple cubic phase with lattice parameter of 144.6 Å; or the (110), (200), (211) and (310) peaks of a body centred cubic phase with lattice parameter of 204.5 Å. The d-spacings of the peaks are listed in Table 5.1. After further annealing of the film for another 13 hours, as shown in Figure 5.3, the first peak disappeared but the other three got stronger and much sharper but with the same *d*-spacings. Thin film, prepared from chloroform solvent using the same procedure, shows no birefringence under polarized optical microscope. This is expected in fact for a isotropic cubic phase.

Table 5.1 Experimental and calculated d-spacings for the cubic phase of CdS quantum dots covered with dendrons, prepared from chloroform solvent and annealed at 150 C in vacuum oven for 6 hours.

Simple cubic (hk)	$d_{obs.}$-spacing (Å)	$d_{cal.}$-spacing (Å)	Bcc (hk)
(100)	144.5	144.6	(110)
(110)	102.2	102.3	(200)
(111)	83.1	83.5	(211)
(201)	64.7	64.7	(310)
Simple cubic *a* = 144.6 Å	Body centred cubic *a* = 204.5 Å		

The size of the CdS quantum dots (including the inner corona) have been determined by TEM as 3.9 ± 4.0 nm, and the diameter of spherical assembly of pure dentrons is 9.8 nm (The data was obtained from Prof. Atsushi Muramatsu's group in the Tohoku University), it would be more reasonable to choose simple cubic with lattice parameter of 14.5 nm as the right phase in comparison. As if in body centred cubic structure, assuming there are two quantum dots in the unit cell, then the distance between them would be 17.7 nm, much bigger than the expected size of the CdS quantum dots plus outer corona. But on simple cubic, the distance between the two quantum dots would be 13.7, reasonably matching the dimensions of the quantum dots and that of the dendrons.

The GISAXS diffraction pattern of the film, after annealing for 19 hours (Figure 5.3) also shows partial orientation, demonstrated by the uneven distribution of intensities along each diffraction ring. Compared with experimental data, the expected orientation of diffraction peaks are about right for simple cubic structure as shown in

Figure 5.3a. However, the combinations of these reflections for BCC do not fit so well as shown in Figure 5.3b.

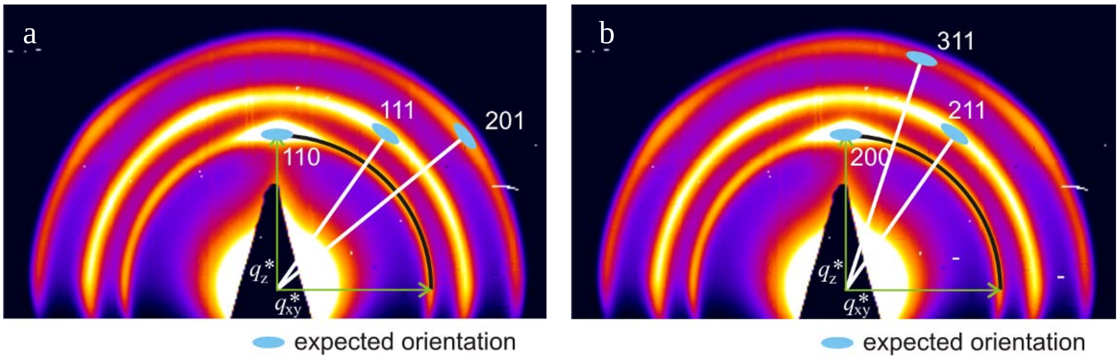

Figure 5.3 GISAXS pattern of simple cubic structure of quantum dots CdS covered with dendrons prepared from chloroform solvent annealed at 150 C in vacuum oven for 19 hours with expected orientation shown a) supposed simple cubic orientation b) supposed body-centred orientation

Table 5.2 Experimental and calculated d-spacings for the cubic phase of CdS covered with dendrons prepared from chloroform solvent annealed at 150 C in vacuum oven for 19 hours

Simple cubic (hk)	$d_{obs.}$-spacing (Å)	$d_{cal.}$-spacing (Å)	Bcc (hk)
(110)	99.3	99.3	(200)
(111)	81.3	81.1	(211)
(201)	62.6	62.8	(310)
Simple cubic a = 140.4 Å		Body centred cubic a = 198.6 Å	

The proposed model of the simple cubic arrangement of CdS covered with dendrons, based on the GISAXS result, is shown in Figure 5.4. The inner core was composed of CdS quantum dots with inner corona attached and the the outer corona consisted of dendrons. The diameter of the aggregate is ~14nm in correspondence with unit cell parameter.

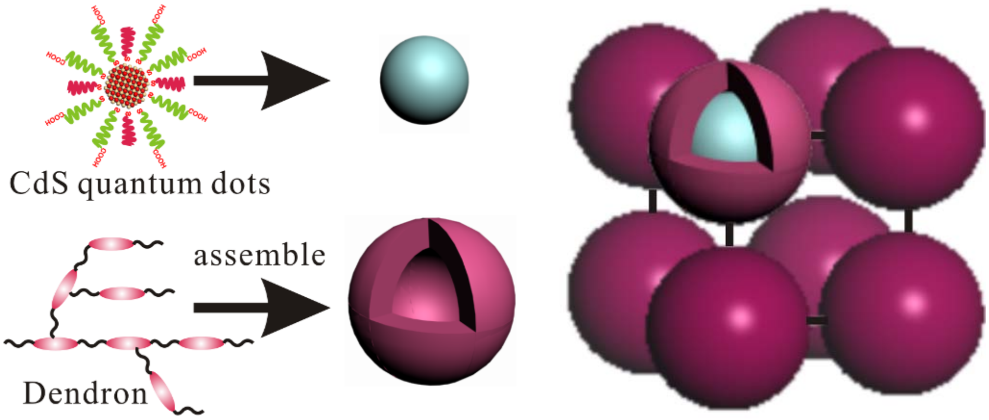

Figure 5.4 Proposed model of simple cubic structure of CdS quantum dots covered with dendrons.

However, why the first reflection (100) was so weak and even gone after long annealing, and why (200) was not observed at all, still remain unresolved at the moment.

Like in dendron-modified gold nanoparticles before,[32] where the gold nanoparticles were assembled on ordered simple cubic structure with space group $Pm\bar{3}m$, self-assembly of QDs covered by LC forming monodendrons have been observed to give rise to an apparent 3-D simple cubic phase as well.

Chapter 6 Self-Assembly of Triangular Pyridine-Au $[C14\text{-}Py\text{-}Au]_3$

6.1 Introduction

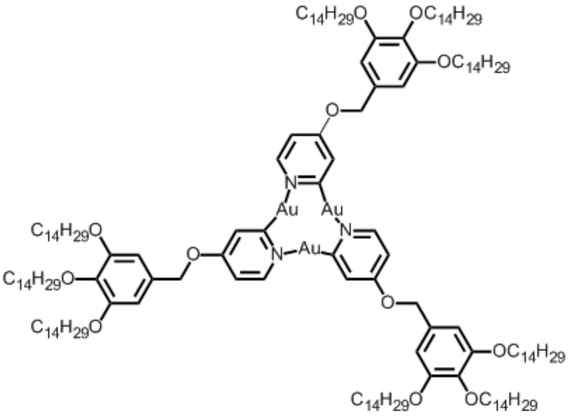

Figure 6.1 Molecular structure of the triangular Pyridine-Au $[C14\text{-}Py\text{-}Au]_3$ (Appreciate the samples provided by Prof. Georg H. Mehl's group in the University of Hull).

In this chapter, instead of covering gold nanoparticles with mesogens, we examine the self-assembly of a disc-like molecule which contains three gold atoms in its core. The molecular structure of the compound, triangular Pyridine-Au $[C14\text{-}Py\text{-}Au]_3$ is shown in Figure 6.1, which has a planner structure suitable for the formation of columnar mesophases. The alkyl chains at the terminal ends are used to help enhance mobility and miscibility of the molecules.

6.2 SAXS results and discussions

The powder x-ray diffraction was carried out on our lab machine. The diffraction pattern at 35 °C is shown in Figure 6.2a below and can be easily indexed to a hexagonal columnar lattice, with lattice parameter a = 42.8 Å. The measured d-spacings are compared with that calculated from best-fit lattice parameter in Table 6.1. After longstanding at room temperature for 1 month, no change in the SAXS pattern has been observed.

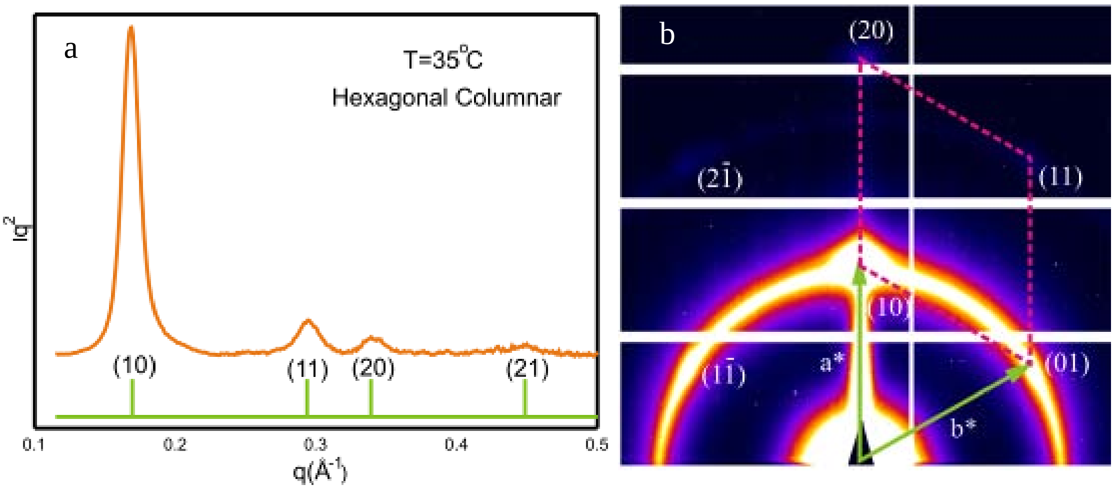

Figure 6.2 a) SAXS powder diffractograms of the hexagonal columnar phase of the compound at 35 °C. The expected peak positions are indicated below the experimental curve. b) GISAX pattern of a oriented thin film in the columnar hexagonal phase, also recorded at 35 °C. The indices of the observed reflections are indicated, with also part of the reciprocal lattice overlaid on top.

The GISAXS pattern, on a thin film prepared from melt on silicon substrate, is shown in Figure 6.2b. A 2D lattice with hexagonal symmetry is clearly seen, the plane group of the group is most likely *p6mm*. On heating the phase goes isotropic around 80°C.

Table 6.1 Experimental and calculated d-spacings for the Col$_{hex}$/*p6mm* phase of the compound recorded at 35 °C

(hk)	$d_{obs.}$-spacing (Å)	$d_{cal.}$-spacing (Å)	*Multiplicity*	*Intensity* (10^{-4})	*Phase*
(10)	37.2	37.1	6	100.0	0
(11)	21.3	21.4	6	10.3	0
(20)	18.4	18.5	6	4.0	0
(21)	14.0	14.0	12	1.5	0
a = 42.8 Å					

6.3 POM results and discussions

As shown in Figure 6.3a, when a thin film is prepared, Schlieren texture could be observed (the black area is due to the bubbles). Such behaviour has been observed for homeotropically aligned columnar phases, due to the orientation variation of the tilt direction. After longstanding at room temperature, more typical columnar texture with larger uniaxial domains was observed, which further confirms the columnar nature of the phase.

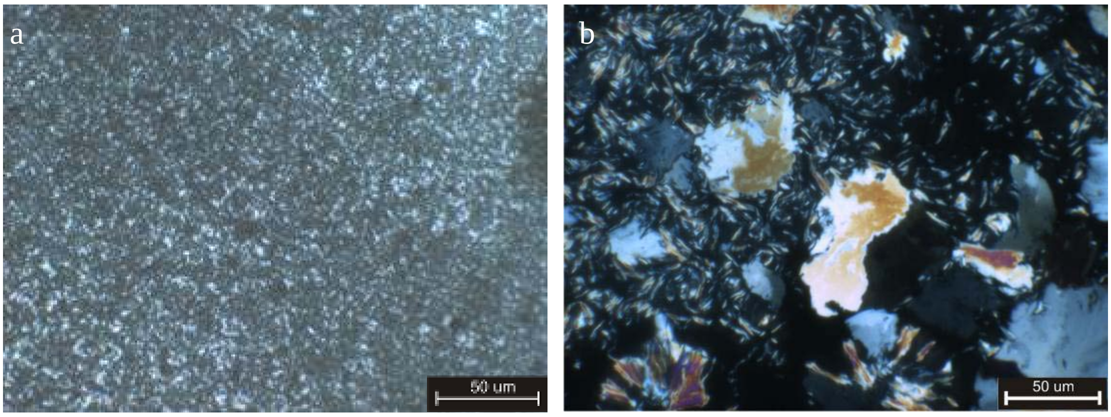

Figure 6.3 Textures of the phase of $[C14\text{-}Py\text{-}Au]_3$ recorded using polarized optical microscope. a) Cooled from isotropic phase at 80 °C to 35 °C with the cooling rate of 1 °C/min b) After longstanding (1 month) at room temperature.

6.4 Reconstruction of electron density map

Diffraction intensities measured by Origin^{TM} software from powder diffraction pattern are used to reconstruct the electron density map (Figure 6.4) of this columnar hexagonal phase. Four peaks are used here to determine the electron density map based on the unit cell parameters and space group information. During this process, the multiplicities of different reflections are also taken into account as listed in Table 6.1. So the number of all the possible phase would be $2^4 = 16$. As shown in Figure 6.3, sixteen distinct electron density maps were generated with all different combinations.

It was obvious to notice that the pairs of phase combinations, (0000), (π000), (0π00), (00π0), (000π), (ππ00), (π0π0) and (π00π) are simply the inverse of (ππππ), (0πππ), (π0ππ), (ππ0π), (πππ0), (00ππ), (0π0π) and (0ππ0). So the number of total electron density maps could be reduced by half to eight.

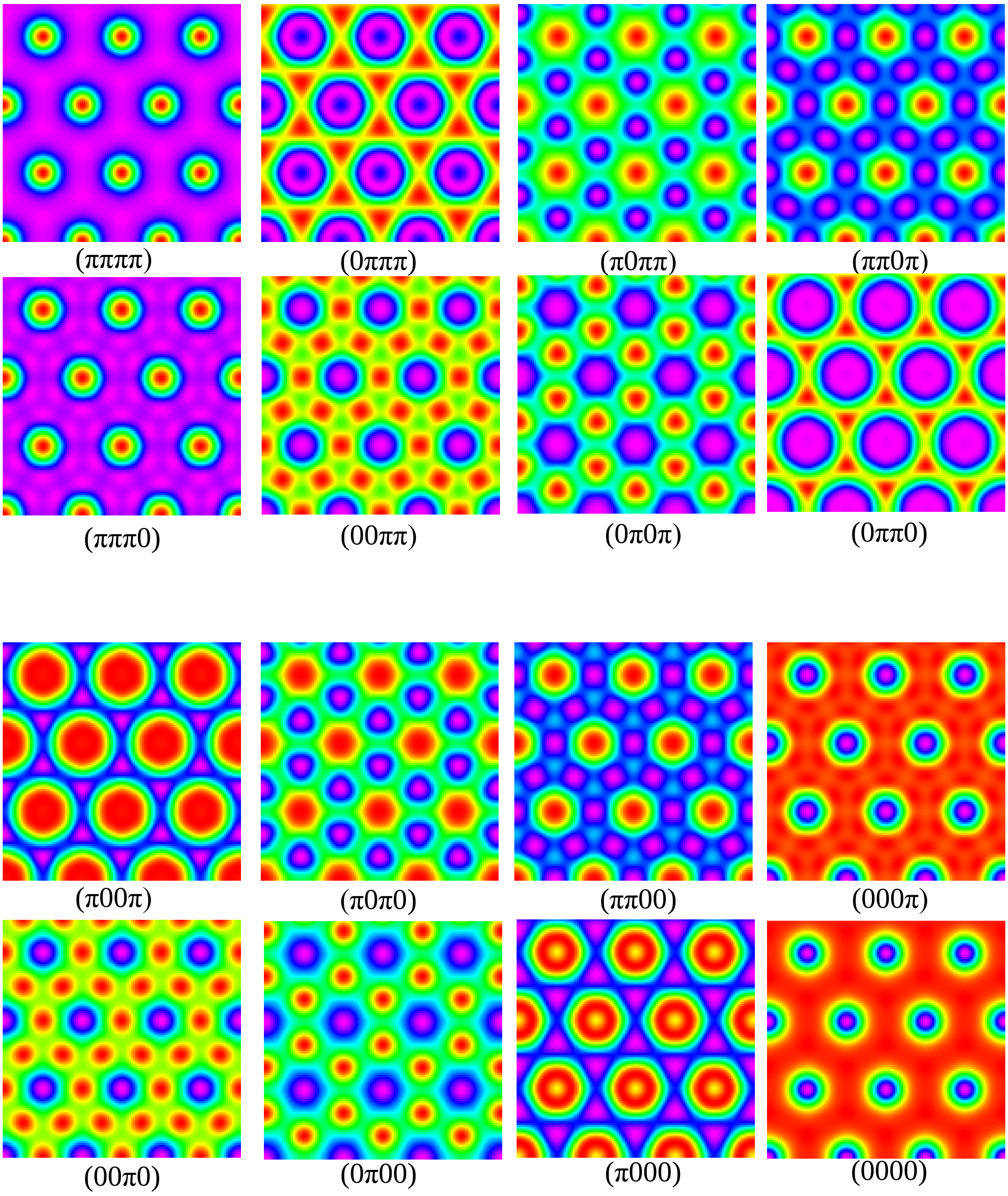

(ππππ) (0πππ) (π0ππ) (ππ0π)

(πππ0) (00ππ) (0π0π) (0ππ0)

(π00π) (π0π0) (ππ00) (000π)

(00π0) (0π00) (π000) (0000)

Figure 6.4 All possible phase combinations of reconstructed electron density maps of Col_{hex} phase of gold Triangular Pyridine-Au $[\mathrm{C14\text{-}Py\text{-}Au}]_3$

Besides, the gold atoms had the highest electron density and should be located in the inner of the core shell structure. So the combinations (π00π), (π0π0), (ππ00) and (π000), where the center was not with the highest electron density, could be excluded.

Now the number was reduced to four. Based on the volume section of each part, the highest electron density part, gold atoms, took up the lowest volume while the lowest electron density part, alkyl chains, occupied the highest. So the phase combination (000π) and (0000) remain. Finally, since the alkyl chains move randomly, the electron density should be evenly distributed and keep the circle shape. So phase (0000) should be the correct one.

In the selected electron density map (Figure 6.5), the circular low electron density areas, red, yellow and green, are located surrounding the puple area, the highest electron density area.

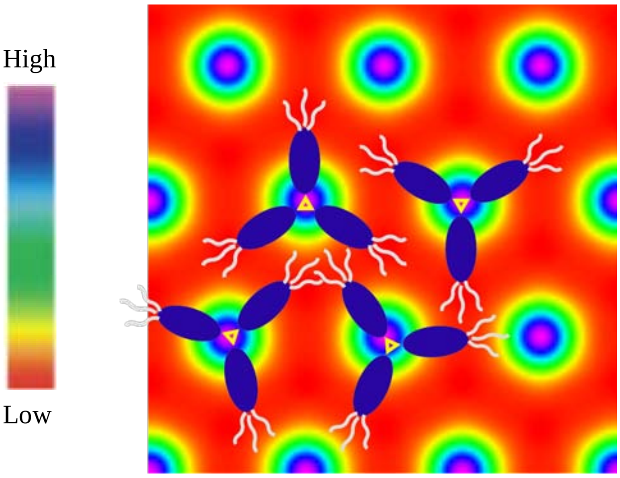

Figure 6.5 Electron density map of triangular Pyridine-Au [C14-Py-Au]3 with a schematic molecular model overlaid on top

As the aromatic cores have the higher electron density so it’s reasonable to assume the gold atoms would take up the purple area while the alkyl chains are located surrounding the gold atoms.

Based on the equation 2.23, the unit cell volume could be calculated from the lattice parameter a_{hex} = 42.8 Å, assuming a height of c = 4.5 Å (average stacking distance) and we obtain V_{cell} = 7139 Å^3. Assumed density ρ = 1.0 g/ml, for the triangular Pyridine-Au [C14-Py-Au]$_3$ ($C_{162}H_{282}Au_3N_3O_{12}$) the number of molecules in a unit cell is 2.4.

Based on the unit cell parameters, molecules numbers and the locations of molecules in the hexagonal lattice, a molecular model of the columnar hexagonal phase has been constructed and molecular dynamic simulation also carried out using Materials Studio. A snapshot of the molecular model during molecular dynamics simulation is shown below in Figure 6.6. The simulation confirms that reasonable space filling and separation of different moieties are achieved in the proposed structure.

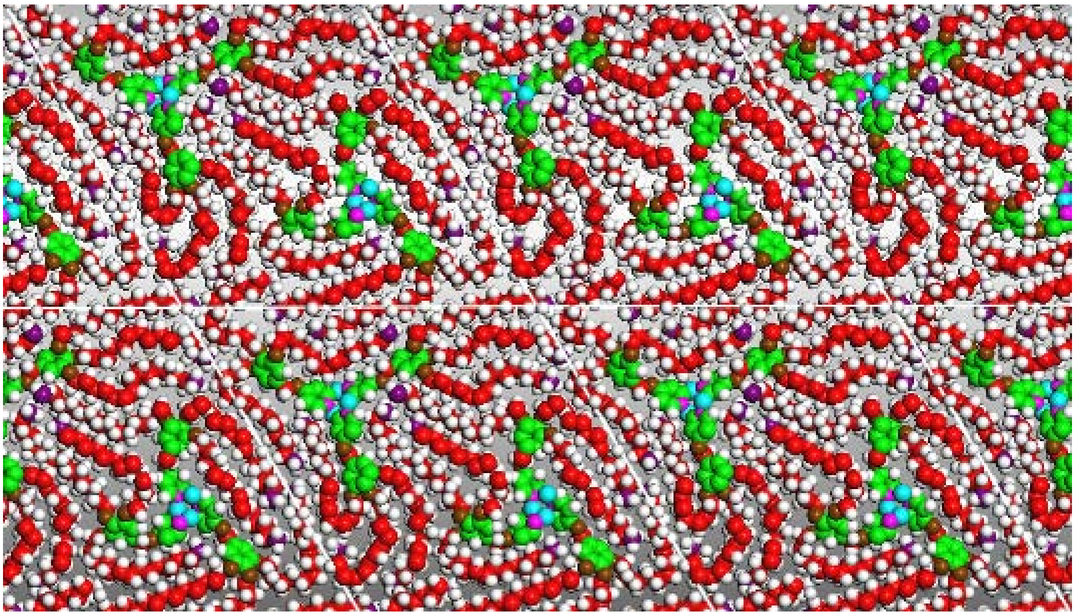

Figure 6.6 Snapshot of a molecular dynamics simulation, colour coding is: blue = gold atomes; green = aromatic cores; red and white = alkyl chain and spacers

6.5 Conclusion

A columnar hexagonal (Col_{hex}) liquid crystal (a = 42.8 Å) is found at 35 °C. The hexagonal symmetry of the liquid crystal phase is confirmed by the GISAXS pattern on an oriented thin film. The texture under the POM changes from Schlieren texture immdiatedly cooled from isotropic, to a fan-shape columnar texture after longstanding at room temperature.

Summary

In summary, nanoparticles covered with hemi-phasmids, rod-like molecule and gold triangle have been investigated by Small-angle X-ray Scattering (SAXS), Grazing Incidence Small-angle X-ray Scattering (GISAXS) and Polarized Optical Microscopy (POM). The combination of SAXS, GISAXS and POM techniques has shown powerful potential as an efficient way to study liquid crystal structures. In this thesis, nanostructures including 1-D lamellar and 2-D hexagonal columnar structures were found and electron density maps were reconstructed based on the integrated diffraction intensities. According to reconstructed electron density maps and molecular information, models of nanoparticles functionalized with mesogens in each structure were proposed.

In the nanoparticles functionalized with hemi-phasmids, under the driving force provided by the parallel alignment of the anisometric mesogens and free movement of the flexible chains, nanoparticles could gradually form long-range order on the mesoscale. For the hemi-phasmidic dimer, a columnar hexagonal ($\mathrm{Col}_{\mathrm{hex}}$) liquid crystal (a = 47.9 Å) is found on cooling of the sample from isotropic phase. The hexagonal symmetry of the liquid crystal phase is confirmed by the GISAXS pattern on an oriented thin film. However, no liquid crystal phase could be obtained for silsesquioxane cages covered with hemi-phasmids. Only broad diffraction peaks, attributed to the isotropic phases, can be observed. The SAXS patterns are similar to those of phasmidic dimer recorded above 50 °C, a demonstration of the similarity in molecular structure between the two compounds. For the gold nanoparticles functionalized with hemi-phasmids, a columnar hexagonal (a= 88.9 Å) phase is found, the order of it improves by cooling slowly from the isotropic phase (above 100 °C). The new columnar hexagonal phase is different from that found in phasmidic dimer as the unit cell parameter is nearly twice of that in the dimer.

In the DBCH compounds, it may be concluded that two different crystalline states and a Smectic-C phase with a thickness of the smectic layer a = 36.9-38.1 Ǻ, depending on temperature, was observed. Finally, in the triangular Pyridine- Au, a columnar hexagonal (a= 42.8 Å) phase is found, confirmed by both SAXS on a powder sample and GISAXS on an oriented thin film. Interestingly, the schlieren texture under POM is observed on a thin film, which could be explained due to the orientation variation of the tilt direction on homeotropically aligned columnar phases.

Future Work

Self-assembly of nanoparticles functionalized with mesogens has shown great potential as an efficient method to arrange spherical nanoparticles into ordered 2-D and 3-D structures. Based on the current results that nanoparticles could be driven under the assembly of mesogens to pack, these progresses could be used to guide the design of functionalized nanoparticles. However, some problems and challenges still remain unsolved such as the missing diffraction peaks in simple cubic phase of dendronized quantum dots. There are many interesting ideas to be tried out such as grafting chiral mesogens onto nanoparticles to see the effects. Theoretical studies have shown the possibility in chiral packing of nanoparticles generating amazing optical properties. And it would be interesting to test if chrial packing of nanoparticles would come true through self-assembly. Besides, research on grafting mesogens onto quantums dots of different size would also be interesting, and coating different mesogens are also required to understand the interaction between the nanoparticles and mesogens for potential optical applications.

Reference

1. Stegemeyer, H., *Liquid Crystals*. 1994: Steinkopff.
2. Liu, F., *Complex supramolecular self-assembly of T- and X-shaped amphiphiles*, 2009, University of Sheffield
3. Chandrasekhar, S., *Liquid Crystals*. 1992: Cambridge University Press.
4. Collings, P.J., *Liquid Crystals: Nature's Delicate Phase of Matter*. 2002: Princeton University Press.
5. Hegmann, T., H. Qi, and V.M. Marx, *Nanoparticles in liquid crystals: Synthesis, self-assembly, defect formation and potential applications.* Journal of Inorganic and Organometallic Polymers and Materials, 2007. **17**(3): p. 483-508.
6. Percec, V., J. Heck, and G. Ungar, *Liquid-crystalline polymers containing mesogenic units based on half-disk and rodlike moieties. 5. Side-chain liquid-crystalline poly(methylsiloxanes) containing hemiphasmidic mesogens based on 4-[[3,4,5,-tris(alkan-1-yloxy)benzoyl]oxy]-4'-[[p-(propan-1-yloxy)benzoyl]oxy]biphenyl groups.* Macromolecules, 1991. **24**(17): p. 4957-4962.
7. Sauer, C., et al., *Smectic, columnar and cubic mesophases in binary systems of hemiphasmidic and calamitic amphiphilic diols.* Liq. Cryst., 1998. **25**(1): p. 109-116.
8. Zeng, X., et al., *Testing the triple network structure of the cubic Im3m (I) phase by isomorphous replacement and model refinement.* J. Mater. Chem., 2008. **18**(25): p. 2953-2961.
9. Boettcher, S.W., et al., *Tunable electronic interfaces between bulk semiconductors and ligand-stabilized nanoparticle assemblies.* Nature Materials, 2007. **6**(8): p. 592-596.
10. Eustis, S. and M.A. El-Sayed, *Why gold nanoparticles are more precious than pretty gold: Noble metal surface plasmon resonance and its enhancement of the radiative and nonradiative properties of nanocrystals of different shapes.* Chemical Society Reviews, 2006. **35**(3): p. 209-217.
11. Shalaev, V.M., et al., *Negative index of refraction in optical metamaterials.* Optics Letters, 2005. **30**(24): p. 3356-3358.
12. Valentine, J., et al., *Three-dimensional optical metamaterial with a negative refractive index.* Nature, 2008. **455**(7211): p. 376-U32.
13. Whitesides, G.M. and B. Grzybowski, *Self-assembly at all scales.* Science, 2002. **295**(5564): p. 2418-2421.
14. Park, S.Y., et al., *DNA-programmable nanoparticle crystallization.* Nature, 2008. **451**(7178): p. 553-556.
15. Hess, B., *Periodic patterns in biology.* Naturwissenschaften, 2000. **87**(5): p. 199-211.
16. Hegmann, T., H. Qi, and V. Marx, *Nanoparticles in Liquid Crystals: Synthesis, Self-Assembly, Defect Formation and Potential Applications.* J. Inorg. Organomet. Polym. Mater., 2007. **17**(3): p. 483-508.
17. Dintinger, J., et al., *A Self-Organized Anisotropic Liquid-Crystal Plasmonic Metamaterial.* Advanced Materials, 2013. **25**(14): p. 1999-2004.
18. In, I., et al., *Spontaneous one dimensional arrangement of spherical Au nanoparticles with liquid crystal ligands.* Chemical Communications, 2005(6): p. 800-801.
19. Kumar, S., et al., *Novel conducting nanocomposites: synthesis of triphenylene-covered gold nanoparticles and their insertion into a columnar matrix.* Soft Matter, 2007. **3**(7): p. 896-900.

20. Marx, V.M., et al., *Bent-core liquid crystal (LC) decorated gold nanoclusters: synthesis, self-assembly, and effects in mixtures with bent-core LC hosts.* Journal of Materials Chemistry, 2008. **18**(25): p. 2983-2994.
21. Skarabot, M., et al., *Two-dimensional dipolar nematic colloidal crystals.* Physical Review E, 2007. **76**(5).
22. Musevic, I., et al., *Two-dimensional nematic colloidal crystals self-assembled by topological defects.* Science, 2006. **313**(5789): p. 954-958.
23. Mang, X., *Self-Assembled Liquid Crystal Nanostructures.*, 2012, University of Sheffield.
24. Cseh, L. and G.H. Mehl, *Structure-property relationships in nematic gold nanoparticles.* J. Mater. Chem., 2007. **17**(4): p. 311-315.
25. Hukins, D.W.L., *X-ray Diffraction by Disordered and Ordered Systems*. 1981: Pergamon Press.
26. Mang, X., et al., *Control of anisotropic self-assembly of gold nanoparticles coated with mesogens.* J. Mater. Chem., 2012. **22**(22): p. 11101–11106.
27. Saez, I.M. and J.W. Goodby, *Chiral nematic octasilsesquioxanes.* J. Mater. Chem., 2001. **11**(11): p. 2845-2851.
28. Saez, I.M., J.W. Goodby, and R.M. Richardson, *A Liquid-Crystalline Silsesquioxane Dendrimer Exhibiting Chiral Nematic and Columnar Mesophases.* Chem. Eur. J., 2001. **7**(13): p. 2758-2764.
29. Dierking, I., *Textures of Liquid Crystals*. 2003: Wiley-VCH.
30. Shen, Z., M. Yamada, and M. Miyake, *Control of Stripelike and Hexagonal Self-Assembly of Gold Nanoparticles by the Tuning of Interactions between Triphenylene Ligands.* Journal of the American Chemical Society, 2007. **129**(46): p. 14271-14280.
31. Donnio, B., et al., *Dendronized ferromagnetic gold nanoparticles self-organized in a thermotropic cubic phase.* Advanced Materials, 2007. **19**(21): p. 3534-+.
32. Kanie, K., et al., *Simple Cubic Packing of Gold Nanoparticles through Rational Design of Their Dendrimeric Corona.* J. Am. Chem. Soc., 2012. **134**(2): p. 808-811.
33. Bragg, W. and W. Bragg, *The reflection of X-rays by crystals.* Proceedings of the Royal Society of London. Series A, 1913. **88**(605): p. 428-438.
34. Weaver, R., *Rediscovering polarized light microscopy.* American laboratory, 2003. **35**(20): p. 55-61.
35. Avery, I.T., *Interference Colour Chart*. 2011: Cel Publishing.
36. Hahn, T., et al., *International tables for crystallography*. 2005: D. Reidel Publishing Company.
37. Imai, M., et al., *Static and dynamic structures of spherical nonionic surfactant micelles during the disorder-order transition.* The Journal of Chemical Physics, 2005. **122**(4): p. -.
38. Zeng, X., et al., *3D Ordered Gold Strings by Coating Nanoparticles with Mesogens.* Adv. Mater., 2009. **21**(17): p. 1746-1750.
39. Zeng, X.B., et al., *Supramolecular dendritic liquid quasicrystals.* Nature, 2004. **428**(6979): p. 157-160.

Appendix An example on how to choose the right electron density map

1.1 The structure of the molecule

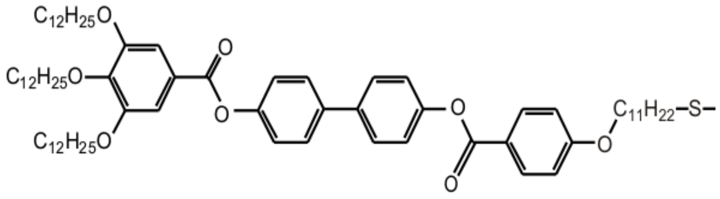

Figure 1.1 Molecular structure of attached hemiphasmid to the gold nanoparticles

Table 1.1 Electron density of each part of the hemiphasmid

Name	Volume (A^3)	Numbers of Electrons	Electron Density (nm^3)
Gold nanoparticle	18.28	79	4322
alkyl chain ($C_{36}H_{78}$)	648	294	454
Aromatic core ($C_{26}H_{14}O_8$)	425	234	551
Spacer ($C_{11}H_{23}S$)	211	105	498

1.2 SAXS data

The molecular length (L) of attached hemiphasmidic mesogen in their most extended conformation spanning between alkyl chains and thiol group in the terminal ends was 57.1 Å. Added by the diameter of nanoparticles 20 Å, the distance between two nanoparticles was 134.3 Å ($a < L < 2a$). Therefore, the attached hemiphasmidic molecule should fold back to be arranged in the unit cell.

Table 1.2 Experimental and calculated d-spacings for the Col_{hex} phase of gold nanoparticles covered with hemiphasmidic mesogens recorded at 37 °C

(hk)	$d_{exp.}$-spacing (Å)	$d_{cal.}$-spacing (Å)	Intensity	Multiplicity
(10)	77.3	77.0	100	6
(11)	44.0	44.5	19.8	6
(20)	38.9	38.5	6.2	6
(21)	28.7	29.1	1.9	12
(31)	21.3	21.4	4.2	12
a=88.9 Å				

1.3. Determination of the phase

As listed in Table 1.2, five peaks was obtained from SAXS experiment. As the intensities of the last two peaks (21) and (31) are not accurate enough to measure, the first three peaks are used here to determine the phase combinations. So the number of all the possible phase would be $2^3 = 8$. As shown in Figure 1.2, eight distinct electron density maps were generated with all difference combinations.

It was obvious to notice that the pairs of phase combinations, (000), (π00), (0π0) and (ππ0) are simply the inverse of (πππ), (0ππ), (π0π) and (00π). So the number of total electron density maps could be reduced by half to four.

As compared in Table 1.1, the gold nanoparticles had the highest electron density and should be located in the inner of the core shell structure. So the combinations (π00), and (ππ0), where the center was not with the highest electron density, could be excluded. Now the number was reduced to two. Based on the volume section of each part, the highest electron density part, gold nanoparticles, took up the lowest volume while the lowest electron density part, alkyl chains, occupied the highest. So the phase combination (000) should be the right one.

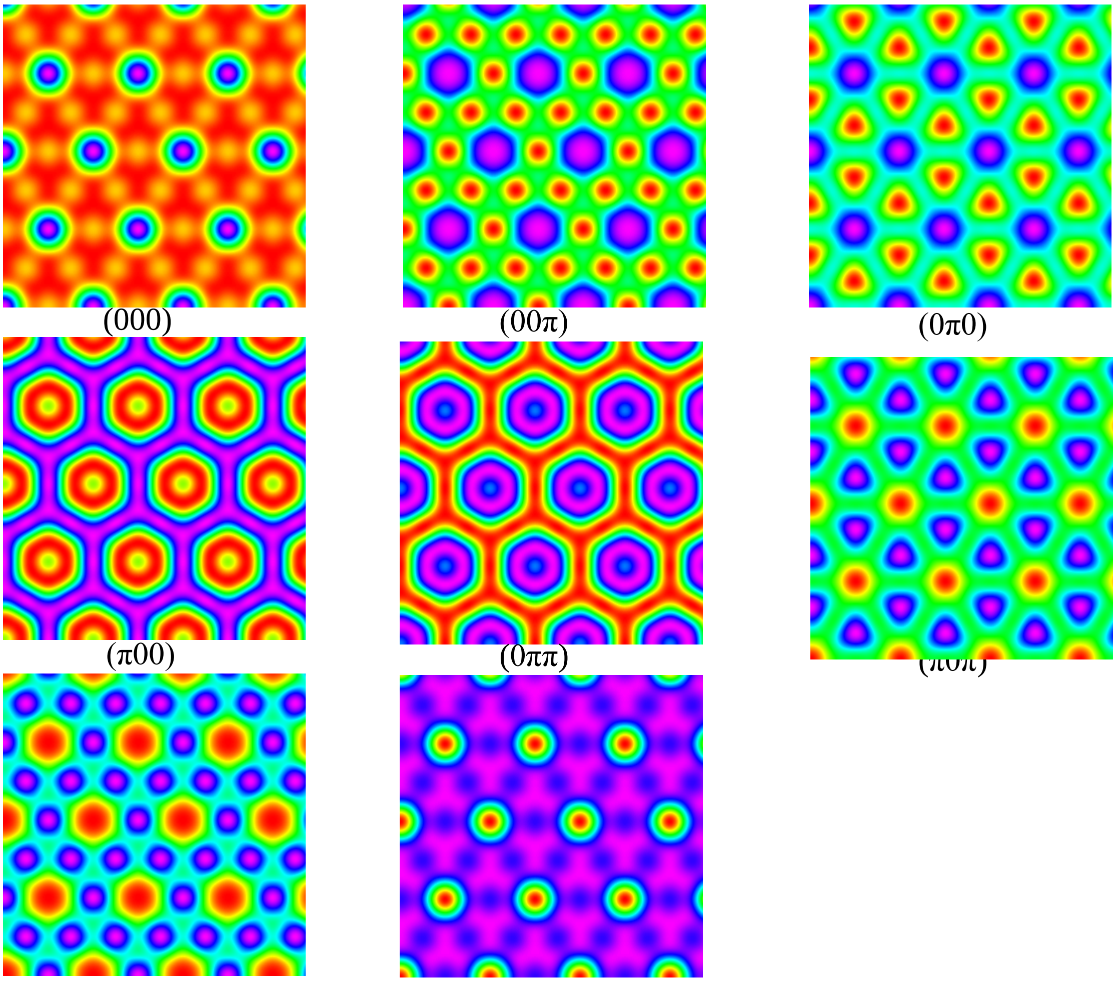

(000) (00π) (0π0)
(π00) (0ππ) (π0π)
(ππ0) (πππ)

Figure 1.2 All possible phase combinations of reconstructed electron density maps of Col_{hex} phase of gold nanoparticle covered with hemiphasimidic mesogen